

Environmental cluster effects and galaxy evolution: The HI properties of the Abell clusters A85/A496/A2670

M. M. López-Gutiérrez,^{1*} H. Bravo-Alfaro,¹ J. H. van Gorkom,² C. A. Caretta,¹ F. Durret,³ L. M. Núñez-Beltrán,¹ Y. L. Jaffé,⁴ M. Hirschmann,^{5,6} D. Pérez-Millán,^{1,7}

¹Departamento de Astronomía, Universidad de Guanajuato, Gto. 36000, México

²Department of Astronomy, Columbia University, New York, NY 10027, USA

³Sorbonne Université, CNRS, UMR 7095, Institut d'Astrophysique de Paris, 98bis Bd Arago, 75014, Paris, France

⁴Inst. de Física y Astronomía, Fac. de Ciencias, Universidad de Valparaíso, Avda. Gran Bretaña 1111, Casilla 5030, Valparaíso, Chile

⁵Institut de Physique, Laboratoire d'astrophysique, École Polytechnique Fédérale de Lausanne (EPFL), CH-1290 Versoix, Switzerland

⁶INAF - Osservatorio Astronomico di Trieste, via G. B. Tiepolo 11, I-34143 Trieste, Italy

⁷Instituto de Radioastronomía y Astrofísica, UNAM, 58089, México

Accepted XXX. Received YYY; in original form ZZZ

ABSTRACT

We study the impact of local environment on the transformation of spiral galaxies in three nearby ($z < 0.08$) Abell clusters: A85/A496/A2670. These systems were observed in HI with the Very Large Array, covering a volume extending beyond the virial radius and detecting 10, 58, 38 galaxies, respectively. High fractions (0.40–0.86) of bright spirals [$\log(M_*/M_\odot) = 9 - 10$] are not detected in HI. We provide further evidence of environmental effects consisting in significant fractions (0.10–0.33) of abnormal objects and a number of red (passive) spirals, suggesting an ongoing process of quenching. Ram-pressure profiles, and the sample of the brightest spirals used as test particles for environmental effects, indicate that ram-pressure plays an important role in stripping and transforming late-types. Phase-space diagrams and our search for substructures helped to trace the dynamical stage of the three systems. This was used to compare the global cluster effects *vs.* pre-processing, finding that the former is the dominating mechanism in the studied clusters. By contrasting the global distribution of HI normal *vs.* HI disturbed spirals in the combined three clusters, we confirm the expected correlation of disturbed objects located, on average, at shorter projected radii. However, individual clusters do not necessarily follow this trend and we show that A496 and A2670 present an atypical behavior. In general we provide conclusive evidence about the dependence of the transformation of infalling spirals on the ensemble of cluster properties like mass, ICM density, dynamical stage and surrounding large-scale structure.

Key words: galaxies: evolution — galaxies: neutral hydrogen — galaxies: clusters: individual: (Abell 85/496/2670)

1 INTRODUCTION

For decades, observations have shown that regions of high galaxy-density, such as cluster cores, are dominated by red E/S0 galaxies while blue spirals are more abundant in lower density regions. Large amounts of observational evidence have confirmed the *morphology-density relation* which constitutes one of the clearest evidences of environment playing an important role in galaxy evolution (Oemler 1974; Dressler 1980; Postman & Geller 1984; Dressler et al. 1997; Goto et al. 2003; Poggianti et al. 2009b). This (*nurture*) scenario is in

full agreement with the Λ CDM model of hierarchical formation of structures, where individual galaxies are predicted, and observed to follow the stream from low to high-density environments during their life time. This galaxy migration seems to be tightly correlated with a systematic change of their physical properties such as morphology, gas content, and SF/AGN activity. On the theoretical side many works (De Lucia, Hirschmann, & Fontanot 2019, and references therein) conclude that secular mechanisms and/or conditions at the time of galaxy formation (*nature*) might be more important than environment in driving galaxy evolution. Theoretical models are still trying to reproduce all the observational trends linked with environment. Nowadays

* E-mail: mm.lopezgutierrez@ugto.mx (MMLG)

it is generally accepted that galaxies at low redshifts have been shaped by both, nature and nurture. However the full understanding of the physics behind the galaxy evolution over cosmological timescales remains a very active research field (*e.g.* Peng et al. 2010; Boselli & Gavazzi 2014; Cortese, Catinella, & Smith 2021).

Solving the question of morphology transformation of spirals into lenticulars, through an evolutionary sequence involving starburst/post-starburst phases (*e.g.* Boselli & Gavazzi 2006; Barway et al. 2007; Poggianti et al. 2009a; Paccagnella et al. 2017; Boselli et al. 2022), requires the study along two main axes, the environment being one of them. Studying galaxies within the same cosmic epoch but living in different environments helps to find correlations between galaxy properties and the physical conditions of their local environment (Bahé et al. 2013; Spérone-Longin et al. 2021). The second axis corresponds to the cosmic evolution: the study of galaxy properties as a function of redshift has shown that a short ($\leq 10^8$ yrs) starburst phase occurs, followed by a long term and complex quenching process (Rhee et al. 2020; Cortese, Catinella, & Smith 2021). As a consequence, the fraction of galaxies in the red sequence almost doubled between $z \sim 1$ and $z = 0$, implying a decrease of blue galaxies accompanied by strong morphology evolution (Butcher & Oemler 1978; Fasano et al. 2000; Arnouts et al. 2007).

Several consortia have been actively approaching the question based on large photometric and spectroscopic surveys such as 2dF and SDSS, covering large sky areas and redshift ranges (Lewis et al. 2002; Balogh et al. 2004; Kauffmann et al. 2004; Poggianti et al. 2017). All these efforts have found indisputable evidence for the impact of environment in galaxy evolution (Boselli & Gavazzi 2006, 2014; Cortese, Catinella, & Smith 2021, and references therein). However, understanding the role played by different physical mechanisms exerted under diverse environment conditions constitutes the matter of a very active debate. The involved physical mechanisms are classified in two types, hydrodynamic and gravitational. Hydrodynamic effects concern the stripping of cold/warm interstellar gas (HI and H₂) by the hot intracluster medium (ICM). The ram-pressure stripping (RPS, Gunn & Gott 1972) and the viscous stripping (Nulsen 1982) are the most studied cases. On the other side we have the tidal (gravitational) mechanisms occurring between a galaxy and the cluster potential (Byrd & Valtonen 1990) or among neighbor galaxies (Merritt 1983; Barnes & Hernquist 1996; Walker, Mihos, & Hernquist 1996). These include major mergers, accretion of low-mass satellites, and the accumulation of fast speed encounters between galaxies (the *galaxy harassment*, Moore, Katz, & Lake 1996). The removal of the galaxy halo gas, known as galaxy starvation (*e.g.* Larson, Tinsley, & Caldwell 1980), is predicted to occur either by hydrodynamic or gravitational interactions. Most of these mechanisms are predicted to transform a spiral galaxy into an S0, and it is known that more than one process might act simultaneously on a single galaxy. The *pre-processing* of galaxies occurring within groups infalling towards clusters, seems to be particularly important (Donnari et al. 2021). Groups of galaxies are known to have lower velocity dispersions than clusters, allowing slower and deeper tidal interactions among their members. Several authors (Fadda et al. 2008; Poggianti et al. 2009b) provided substantial evi-

dence that strong galaxy evolution is occurring in low mass systems at large distance from the cluster core. However, the debate *pre-processing vs. cluster effects* remains open because many variables are involved, such as the infalling orbits, initial gas/stellar masses, the group/cluster properties and even the surrounding large scale structure (Salerno et al. 2020; Rhee et al. 2020).

In this context, studying the atomic hydrogen (HI) of spiral galaxies, in combination with observations at other frequencies and with numerical simulations, has proven to be a powerful tool to study galaxy evolution as a function of environment. HI is probably the best tracer of galaxy interactions as it extends well beyond the stellar disk. Several studies have been devoted to the nearest clusters such as Virgo, Hydra, A 1367 and Coma (*e.g.* Giovanelli & Haynes 1985; Cayatte et al. 1990; Bravo-Alfaro et al. 2000; Solanes et al. 2001; Chung et al. 2009; Scott et al. 2010, 2018; Boselli et al. 2021; Wang et al. 2021; Molnár et al. 2022). The large coverage and high sensitive HI-surveys carried out with single dish telescopes, such as HIPASS and ALFALFA (Giovanelli et al. 2005; Haynes et al. 2018), provided statistical information on the HI content of large samples of spirals in different environments. All these surveys have shown that spirals in clusters have systematically less gas than their counterparts in the field. This loss of cold gas is known to be the first step to the eventual quenching of star formation observed in cluster galaxies.

In parallel to single-dish surveys, HI synthesis imaging provides critical information mainly at low redshifts. This technique unveils different types of disruptions like gas shrunk discs, asymmetries, and offsets between the gas and the stellar disks (Bravo-Alfaro et al. 2001; Chung et al. 2009; Scott et al. 2018; Luber et al. 2022, and references therein). HI-maps and kinematical velocity-fields are essential to constrain hydrodynamical simulations of galaxies under different environment processes (*e.g.* Vollmer et al. 2012; Tonnesen 2019, and references therein). With a few remarkable exceptions, HI-synthesis imaging surveys are restricted to the nearby universe ($z < 0.1$) due to instrumental limitations and to the very long observing times required. As a consequence, only a few clusters have been fully covered by using this technique. The new generation of radio telescopes such as ASKAP and MeerKAT (Koribalski et al. 2020; Jonas & MeerKAT Team 2016), as well as upgraded instruments like the Westerbork Synthesis Radio Telescope (WSRT) and the Karl G. Jansky Very Large Array (VLA), are nowadays pushing farther the redshifts of HI-imaged galaxies. The BUDHIES project (Jaffé et al. 2013, 2016; Gogate et al. 2020) use the WSRT to characterize the HI properties in and around two clusters at $z = 0.2$, A963 and A2192. The CHILES project (Fernández et al. 2013; Hess et al. 2019) uses the VLA to image the HI in a 40 arcmin field out to $z = 0.45$ and has made a direct detection at the largest distance so far, at $z = 0.376$ (Fernández et al. 2016). In parallel to pushing the study of HI to higher redshifts (the *time axis*) it is equally important to enlarge the sample of studied clusters lying at the same epoch (the *environment axis*). Large-volume, HI blind imaging surveys like the one presented in this work are intended to explore different clusters from their core to the outskirts. The HI maps and kinematics of resolved objects are studied as a function of the very diverse environments where galaxies are located.

In this paper we enlarge the sample of nearby systems ($z < 0.08$) imaged in HI. Large volumes of the Abell clusters A85, A496, A2670, were homogeneously observed with the VLA. We discuss their global HI properties paying special attention to a complete sample of bright spirals, used as test particles for environment effects. We obtain HI physical parameters of individual galaxies and deliver an atlas of HI maps and velocity fields. Bright spirals not detected in HI are of particular interest. We seek for correlations between gas properties of individual galaxies within the substructures reported in this work as a test quantifying the pre-processing. We present profiles of the ram pressure and projected phase space diagrams (PPS) for each cluster. Finally, we use the gas content and color index as a first approach quantifying the quenching fraction in the studied clusters. In forthcoming papers we will use optical spectra and multi-band observations to complement the study of individual galaxies in particular those showing strong distortions in HI and in optical.

This paper is organized as follows: Section 2 describes the clusters under study, the observations and the data reduction for the HI and the optical imaging. In the same section we describe the catalogues of member objects used in this work, as well as the sample of the brightest spirals and the color-magnitude diagrams of the studied clusters. In Section 3 we give the main observational results: we provide the HI parameters of all detected galaxies and their global distribution across the observed clusters. Tables containing these data and the corresponding HI maps are given in the Appendix. In Sect. 4 we study the dynamical state of the three clusters by applying two independent methods tracing substructures. In Sect. 5 we calculate RPS profiles and we obtain radial velocity *vs.* cluster-centric distance plots in order to study the assembly history of the clusters. In Sect. 6 we compare the clusters with each other and we discuss the role played by the cluster environment in the evolution of infalling galaxies. We summarize our results and give our conclusions in Sec. 7. Throughout this paper we assume $\Omega_M = 0.3$, $\Omega_\Lambda = 0.7$, and $H_0 = 70 \text{ km s}^{-1}\text{Mpc}^{-1}$.

2 THE OBSERVATIONS

2.1 The cluster sample

In this work we study the Abell clusters A85 ($z = 0.055$), A496 ($z = 0.033$), A2670 ($z = 0.076$), which harbor different physical properties (see Table 1) and dispose of ancillary multifrequency data.

A85 is more massive and more luminous in X-rays than the other two systems. Despite its relaxed morphology it is known to be undergoing minor merging processes with a subcluster and groups seen in X-rays and in the optical (Durret et al. 1998; Durret, Lima Neto, & Forman 2005; Bravo-Alfaro et al. 2009). More recently, this system has been confirmed to possess a centrally peaked profile in X-rays with a sloshing pattern (Ichinohe et al. 2015) and with some additional disturbed features (Laganá, Durret, & Lopes 2019). The presence of jellyfish galaxies like JO201 has been associated with strong RPS in this cluster (Ramatsoku et al. 2020; Luber et al. 2022, and references therein).

A496 is known to have a very relaxed morphology (Dur-

Table 1. Properties of the studied clusters

	A85	A496	A2670
RA (2000)	00 41 50	04 33 38	23 54 14
Dec (2000)	-09 18 07	-13 15 33	-10 25 08
z/D_c (Mpc)	0.055/233	0.033/140	0.076/320
D_l (Mpc)	245.4	144.9	344.1
scale $10'$ (Mpc)	0.69	0.41	0.95
v_{cl} (km s $^{-1}$)	16,607	9,884	22,823
σ_{cl} (km s $^{-1}$)	1054	685	781
R $_{200}$ (Mpc)	2.54	1.68	1.86
M $_{200}$ ($10^{14} M_\odot$)	12.6	3.49	5.07
Morph (B-M)	I	I	I-II
Richness	130	134	224
L_X (10^{44} erg^{-1})	9.4	3.8	2.3
LSS	SC (11)	isolated(*)	isolated

Notes:

- D_c (comoving distance), D_l (luminosity distance) and linear scale for $10'$ are estimated with $H_0 = 70 \text{ km s}^{-1}\text{Mpc}^{-1}$.

-The central velocity (v_{cl}), the velocity dispersion (σ_{cl}) and L_X were taken from NED, HyperLeda and BAX, respectively.

-R $_{200}$: computed following Finn et al. (2005).

-M $_{200}$ was estimated following Barsanti et al. (2018).

-LSS (large scale structure): indicates that A85 is part of the supercluster MSCC 039, consisting of 11 cluster members (Chow-Martínez et al. 2014).

(*) We revisit the LSS of A496 in this work.

ret et al. 2000; Boué et al. 2008a; Ulmer et al. 2011) consistent with a significant coincidence between the BCG and the cluster centroid (position and velocity) (Lopes et al. 2018). Nevertheless, Laganá, Durret, & Lopes (2019) reported disturbed features superposed onto a centrally peaked X-ray distribution. Concerning the LSS, A496 was reported as an isolated system by Chow-Martínez et al. (2014). We revisit this result in Sect. 6.

A2670 is the faintest of the three systems in X-rays, however its ICM is not negligible: RPS is blamed for strong sweep of material observed in a post-merger galaxy (Sheen et al. 2017). A2670 is the most irregular of the three systems and displays a very elongated morphology distributed along a NE-SW axis. This cluster is dynamically young, as suggested by the diffuse X-ray emission and the large offset in velocity of 333 km s^{-1} (C. Caretta, priv. comm.) between the cluster and the BCG; this clearly indicates that the massive galaxy has not yet settled at the bottom of the cluster potential well.

2.2 The HI data

We take advantage of HI-data obtained with the VLA¹ between 1994 and 1996 for A2670, and from 2001 to 2003 for A85 and A496. All observations were taken in C configuration, producing beam sizes of $\sim 24'' \times 17''$. Table 2 gives the main observing parameters: the total integration time, the VLA configuration, the beam size, the bandwidth and the correlator mode applied. The correlator mode defines the number of polarizations applied. The correlator mode 1

¹ The National Radio Astronomy Observatory is a facility of the National Science Foundation operated under cooperative agreement by Associated Universities, Inc.

Table 2. HI observational parameters

ID	T_{int} (h)	VLA config.	beam ($''$)	Bandw MHz	Correl. mode
(1)	(2)	(3)	(4)	(5)	(6)
A85	80	C	24×17	6.3	2AC
A496	12	C	25×17	6.3	2AC
A2670	90	C	23×16	12.5	1A, 1D

Column (2): The time on source, in hours.

Column (3): The VLA configuration used.

Column (4): The beam size in arcsec.

Column (5): The applied bandwidth in MHz.

Column (6): The correlator mode.

uses one polarization and allows a larger number of velocity channels; mode 2 applies two polarizations and is able to produce an improvement in sensitivity by a factor of $\sqrt{2}$. Hanning smoothing was used on the data of A85 and A496, obtaining a set of 31 independent channels. For A2670 no Hanning smoothing was applied, obtaining a set of 63 channels (cubes NE and SW). The general observing strategy is based on a combination of several observing pointings at different positions and central velocities. This allowed to cover the full cluster volume beyond one virial radius and more than three times the velocity dispersion. Fig. 1 shows the total observed fields for each cluster and Table 3 gives the parameters of the final HI data cubes. Throughout this paper we list the HI heliocentric velocities using the optical definition.

We applied different observing strategies to each cluster depending on their redshifts and velocity dispersions. Six VLA fields were pointed side by side across A85. The individual fields have slight overlap in RA, Dec in order to avoid any gap in between. These fields have the same central velocity giving a homogeneous coverage across an area of $\sim 100'$ side after a mosaicing procedure (Taylor, Carilli, & Perley 1999). The same six fields were observed three times, each one centered at a different velocity: $15,266 \text{ km s}^{-1}$, $16,500 \text{ km s}^{-1}$, $17,744 \text{ km s}^{-1}$ (see Table 3). The central velocities were chosen to slightly overlap producing a homogeneous coverage of some 3800 km s^{-1} , *i.e.* more than 3.5 times the velocity dispersion of A85.

A similar procedure was applied to A496. Since it is located at two thirds the distance of A85 the total integration time for A496 was significantly reduced. On the other hand this cluster is spread across a larger region of the sky and we had to apply ten VLA pointings with different RA, Dec positions in order to reach the one virial radius coverage. These fields went through a mosaicing procedure delivering a field of view of some $100'$. Having a low velocity dispersion (737 km s^{-1}), the ten fields were observed two times, each one centered at a different velocity: $9,285 \text{ km s}^{-1}$ and $10,429 \text{ km s}^{-1}$. This delivered a coverage of $\sim 2400 \text{ km s}^{-1}$, equivalent to more than 3.5 times the cluster velocity dispersion (Table 3).

A different observing strategy was applied to A2670. Located at a larger distance than the previous clusters, A2670 needed fewer VLA pointing fields to cover the virial radius. However, due to its distance, longer observing time was needed in order to reach a similar detection limit than the other clusters. The one virial radius coverage was en-

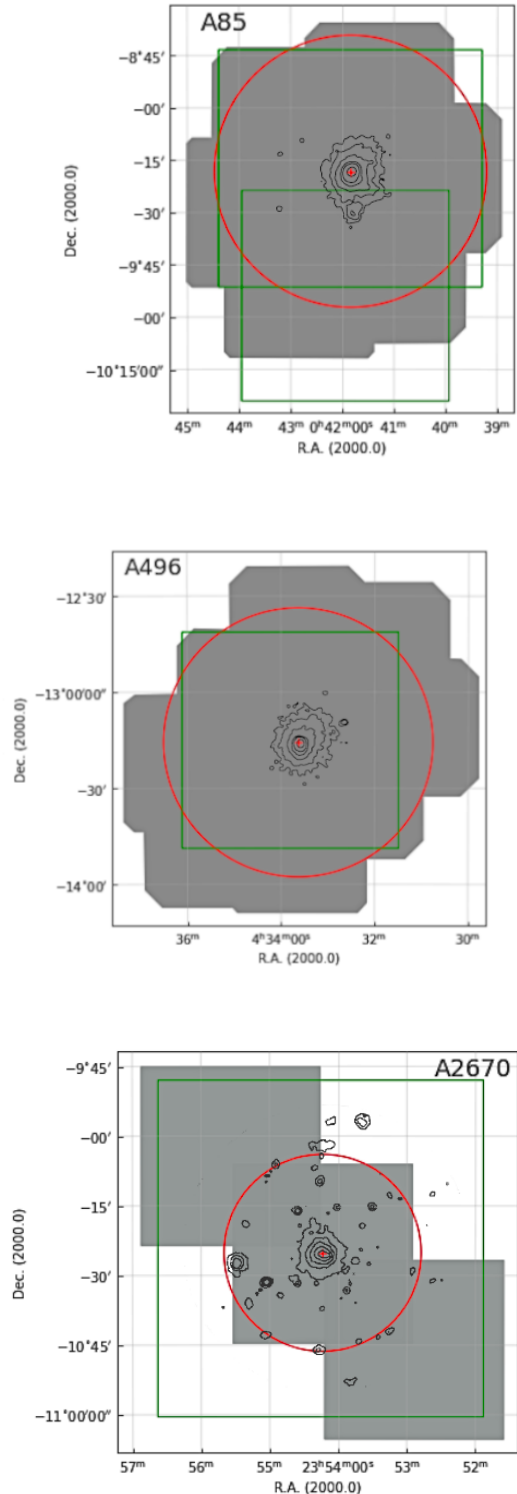


Figure 1. The observed fields in HI (grey polygons) and in optical (green squares). A85 is in the top panel, A496 in the middle, and A2670 in the bottom. The R_{200} radius is indicated with a red circle and the black contours draw the ROSAT X-ray emission. The BCG is indicated with a red cross.

Table 3. The HI-data cubes.

Data cube (1)	RA (2000) (2)	Dec (2000) (3)	FoV ($'$) (4)	Vel. range km s^{-1} (5)	V_c km s^{-1} (6)	Δv km s^{-1} (7)	rms mJy beam^{-1} (8)	M_{HI} limit $10^8 M_{\odot}$ (9)
A85–LV	00 41 51.9	-09 18 17	90	1,366	15,266	45.5	0.25	9.0
A85–MV	00 41 51.9	-09 18 17	90	1,330	16,500	46.9	0.25	9.2
A85–HV	00 41 51.9	-09 18 17	90	1,387	17,744	46.2	0.25	9.1
A496–LV	04 33 04.1	-13 06 19	100	1,314	9,285	43.8	0.24	3.0
A496–HV	04 33 04.1	-13 06 19	100	1,324	10,429	44.2	0.24	3.0
A2670–C	23 54 13.8	-10 25 09	40	4,120	23,037	47.9	0.11	7.9
A2670–NE	23 55 34.1	-10 04 18	40	2,957	22,690	47.7	0.12	8.6
A2670–SW	23 52 53.4	-10 46 00	40	2,957	22,690	47.7	0.12	8.6

Column (1): Field ID, where LV, MV, HV indicates low, medium and high velocity ranges, respectively.

Columns (2) and (3): Central coordinates for the data cube, after mosaicing for A85 and A496.

Column (4): Approximate diameter of the FoV, in arcmin.

Column (5): Total velocity coverage, in km s^{-1} .

Column (6): The heliocentric velocity of the central channel, using the optical definition.

Column (7): Velocity resolution given by the channel width, in km s^{-1} .

Column (8): The rms per channel in mJy beam^{-1} .

Column (9): The HI-mass detection limit, in units of $10^8 M_{\odot}$.

sured by pointing three VLA fields spread along a NE-SW axis and having some overlap in order to avoid any gaps. Due to observing time limitations, the covered area is elongated, giving priority to the NE-SW axis. Mosaicing was not applied in this cluster and the three data cubes were analyzed separately. The velocity coverage was ensured by applying a bandwidth of 12.5 MHz and correlator modes 1A for the central cube, and 1D for the NE and SW cubes. This strategy delivered a central data cube with a coverage of $4,000 \text{ km s}^{-1}$ and nearly $3,000 \text{ km s}^{-1}$ for the NE and SW cubes (Table 3).

Standard VLA calibration and imaging were carried out by using the NRAO Astronomical Image Processing System (AIPS). All final data cubes for A85 and A496 have 31 channels with velocity widths between 43.8 km s^{-1} and 46.9 km s^{-1} . The central field A2670-C has 88 channels while 2670-NE and 2670-SW have 63 channels. All data cubes for this cluster have a channel width close to 48 km s^{-1} . The imaging was made by applying ROBUST=1.0 (Briggs 1995), which is the best compromise between uniform and natural weighting. This maximizes the sensitivity while keeping high spatial resolution, delivering a final beam size of about $24'' \times 17''$ for the three clusters. The typical rms is $\sim 0.24 \text{ mJy beam}^{-1}$ for A85 and A496, while $\sim 0.12 \text{ mJy beam}^{-1}$ was reached for A2670 (see Table 3). This allowed to obtain HI-mass detection limits of the same order of magnitude for the three systems.

The search for detections and the HI analysis were carried out using AIPS. The moment maps were produced with the AIPS task MOMNT, applied with Gaussian (space coordinates) and Hanning smoothing (velocity) to maximize the signal-to-noise ratio. We produced HI-maps and velocity fields using a cutoff level between 1.5 and 2.0 times the rms measured in the corresponding data cube. As expected, variations of noise were found at the edge of the data cubes, in RA, Dec and velocity. We normally discarded detections found within those zones.

2.3 CFHT MegaCam optical images

We obtained optical images with the 3.6m Canada France Hawaii Telescope and the MegaCam instrument, each field having a size of around $1 \times 1 \text{ deg}^2$. The south tip and the infalling filament of A85 were observed in October 2004 (program 04BF02); we exploit here the $u g r i$ band images, with surface magnitude limits of 26.7, 27.3, 26.4, 25.7 mag arcsec^{-2} , respectively. Details can be found in Boué et al. (2008b). We later retrieved archive images, this time centered on A85 in the g and r bands. The corresponding depths are 26.3 and 26.1 mag arcsec^{-2} . We assembled the individual images (five in each band) to obtain frames with total exposure times of 3960s and 8380s.

A496 was observed with the same telescope and instrument (November 2003, program 03BF12) obtaining $u g r i$ band images. The total exposure time is 7853 s for each image and the depths are 27.4, 27.2, 26.2, 25.6 mag arcsec^{-2} , respectively. Details on these data can be found in Boué et al. (2008a).

The data for A2670 were taken from the CFHT archive, with a total exposure time of 6160 s in the $u g r z$ bands. The depths are 25.7, 26.8, 26.3, 24.2 mag arcsec^{-2} , respectively.

2.4 The membership catalogues

We use the spectroscopic redshift compilation by H. Andernach (priv. comm.) to define the member sample of the three clusters. This compilation considers as potential members all galaxies with published radial velocities inside a projected Abell radius ($R_A = 2.1 h_{70}^{-1} \text{ Mpc}$), and within a range of $\sim 2500 \text{ km s}^{-1}$ from a preliminary estimation of the cluster velocity. Several observational limitations could prevent the redshift catalogues to be fully complete within the studied regions; nevertheless it remains the most reliable option with the data currently available in the literature. Taking this redshift sample, the membership catalogues are constructed by tracing caustic curves representing the escape

velocity of the system in a projected phase-space diagram (see, [Serra et al. 2011](#), and references therein for more details). The curves are constructed following [Chow-Martínez \(2019\)](#). All galaxies within the defined limits are taken as cluster members. The caustics applied here are intentionally *relaxed* (an enclosing fit) as the catalogues are intended to retain as many potential member galaxies as possible. The membership catalogues contain 616, 368, 308 objects in A85, A496, A2670, respectively. Due to its larger redshift A2670 is sampled through a larger linear radius. This bias will be taken into account when we compare the observed clusters with each other in Sect. 6.

2.5 Catalog of the brightest spiral galaxies

HI blind surveys covering large cluster volumes allow to study the gas component of all the member galaxies contained within the observed data cubes. Even those spirals not detected in HI are very important as they trace the distribution of HI swept spirals throughout the studied cluster. With this in mind we built catalogues (RA, Dec, v_{rad}) of the brightest spirals contained within the VLA data cubes. As a first step, magnitudes g, r were obtained for all the member galaxies by applying SExtractor² to the CFHT images referred above. A few zones observed by the VLA but not covered by the CFHT (Fig. 1) were similarly analyzed by using Pan-STARRS³ frames ([Flewelling et al. 2020](#)).

The strategy to define the bright spiral catalog is as follows. We applied a limit in apparent magnitude of $g = 19.0, 18.0, 19.5$, for A85, A496, A2670, respectively. Considering the distance to each cluster, these values roughly correspond to the same absolute magnitude, $M_g \sim -18.0$. In r -band this limit is close to $M_r = -18.2$. We convert these magnitudes to stellar mass following [Mahajan et al. \(2018\)](#), showing that our catalogues of bright spirals are complete in mass above a value of $\log(M_*/M_\odot) = 9.0$. We did not apply a color-index threshold in order to include any possible red spiral. This method delivered bright objects whose morphology can be defined through visual inspection; this was done by using combined (RGB) optical images from CFHT and Pan-STARRS. All objects in the blue cloud (see next subsection) and having stellar mass above $\log(M_*/M_\odot) = 9.0$ were considered as candidates to be spiral. Our visual inspection confirmed spiral features for most of those objects. The remaining ones, before being included in the sample of bright spirals, should present a combination of features based on a disk shape, blue ($g - r$) color, stellar mass, HI content, and the presence of dust lanes (for the near edge-on ones). As shown below, a few red spirals are reported in the three clusters. Their belonging to the bright spiral sample was conditioned by the following criteria: having a mass above $\log(M_*/M_\odot) = 9.0$, being detected in HI or, alternatively, showing spiral features through our visual inspection. This output was cross-matched with the list of member objects (Sect. 2.4) in order to ensure that these spirals are cluster members. The final catalogues of bright spirals consist of 65, 46, 61 member objects in A85, A496, A2670, respectively. Hereafter we denote these objects as B-Sp.

² <https://www.astromatic.net/software/sextractor/>

³ <https://panstarrs.stsci.edu/>

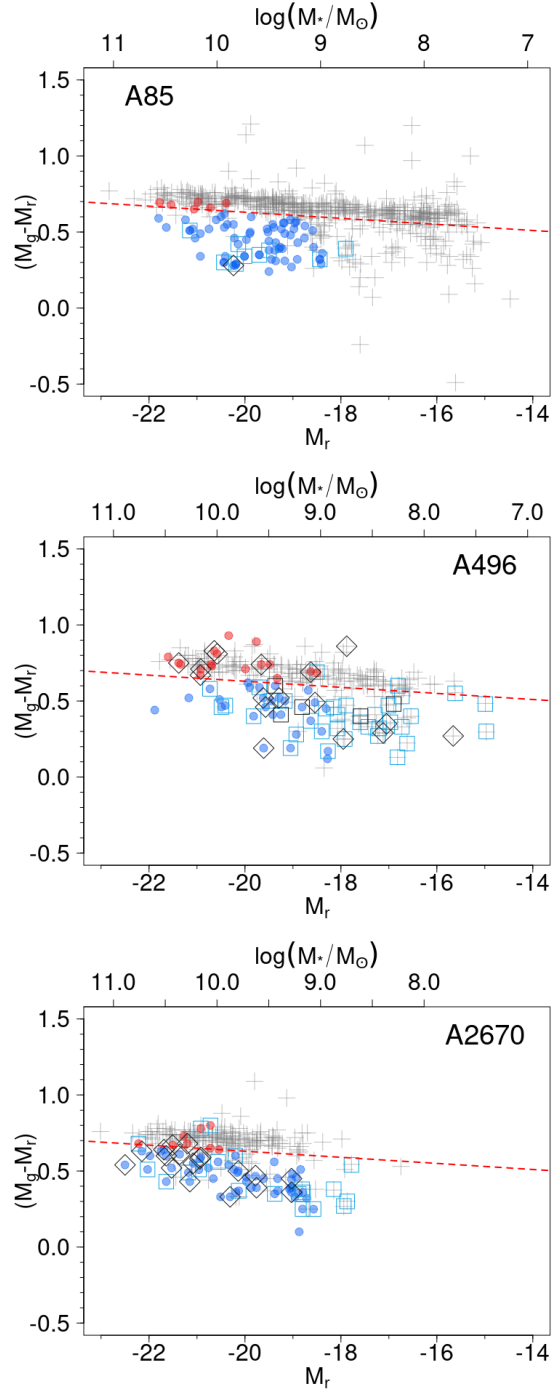


Figure 2. Colour-magnitude diagrams showing cluster members with grey crosses. The red dotted line draws the border between the red sequence and the green valley (see text). The bright spirals are shown with solid circles (blue and red). Squares/diamonds indicate the HI normal/abnormal galaxies (see Sect. 3).

2.6 Color-magnitude diagrams: the galaxy populations

Tracing color-magnitude diagrams (CMD) in a cluster helps to visualize the distribution of different types of galaxies populating the system. Fig. 2 shows the CMD of the three clusters, giving the color index as a function of the absolute magnitude M_r (bottom axis) and stellar mass (upper axis).

The red dotted line draws the border between the red sequence and the green valley; it is defined as: $(g - r) = 0.63 - 0.02(M_r + 20)$ (Masters et al. 2010).

Member galaxies in Fig. 2 are shown with grey crosses. The bright spirals defined in the previous section

are cluster members too; they are indicated with solid circles, either red or blue, indicating their position in the red sequence or in the blue cloud. Cluster members in the red sequence being brighter than $M_r = -18.2$ (*i.e.* mass above $\log(M_*/M_\odot) = 9.0$), and having no solid circle, correspond to early types.

Galaxies above the same mass limit and lying in the blue cloud are confirmed to be part of the B-Sp sample (see previous subsection). The HI detections are shown with blue open squares (normal objects) or with black diamonds (HI-abnormal objects, defined in the next section). A few HI detections are not part of the compilation of member galaxies; either no redshift was available or they are outside the velocity window defined by the membership catalog of Sect. 2.4. We added these objects as new cluster members.

Galaxies located in the blue cloud of these clusters are good candidates to be in a pre-quenching stage. Optical colors are not the best indicators for current star-forming activity due to possible differences between the time scales for quenching and for the change in color due to the stop of star formation. Nevertheless, not having optical spectra for all the objects under study, we consider that a blue color combined with a normal gas content, constitute a reasonable indicator for galaxies in a pre-quenching phase. On the other side, objects above the red line of Fig. 2 are not expected to have any intense star formation activity, therefore red circles in this figure constitute very likely passive spirals. A K-correction was applied to the three clusters. The largest K-correction values in color-index are slightly above 0.1 mag. As expected, these values correspond to red objects in A2670 (we used the K-correction calculator from GAISH⁴). As this correction is associated with the galaxy distance, the y-axis of Fig. 2 shows the difference in absolute magnitudes after the K-correction was applied. Galactic extinction is negligible for these clusters and no correction was applied.

3 RESULTS

3.1 The HI detected galaxies

The catalogues of bright spirals (B-Sp) described above provide positions and velocities that were used to seek for their HI-emission in the corresponding data cubes. Most of these B-Sp were effectively detected in HI but, in all three clusters, significant fractions of these spirals were not detected. These objects constitute our sample of HI non detected spirals. This sample is complete in mass above the limit $\log(M_*/M_\odot) = 9.0$. The search for 21 cm emission was completed by a thorough visual inspection of the HI data cubes. This was done blindly, disregarding all information on optical positions and redshifts of the spiral galaxies. Our search produced a list of emissions, most of them matching in position and velocity with a B-Sp. However, several candidate

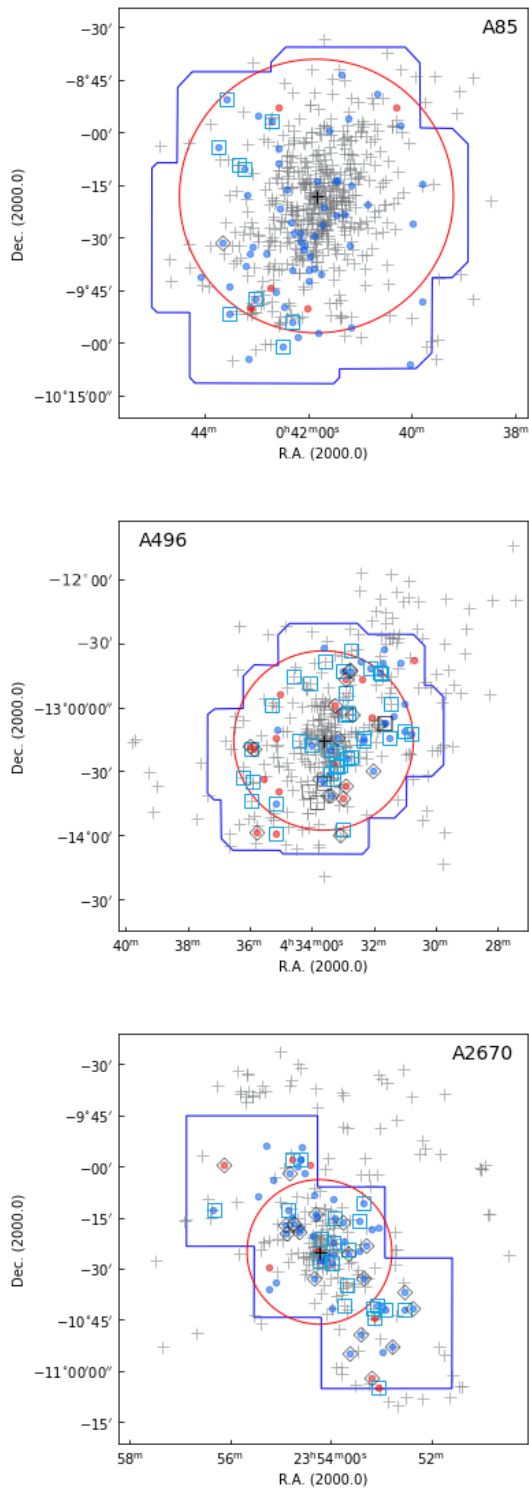


Figure 3. The distribution of member galaxies (grey crosses) in the studied clusters. HI detections are shown with blue squares (normal) and black diamonds (abnormal). Symbols for the bright spirals are the same as in Fig. 2 (blue and red circles). R_{200} is indicated with a red circle and the blue polygon shows the VLA field of view. The cluster center is indicated with a red cross.

⁴ <http://kcor.sai.msu.ru>

detections had no counterpart in the B-Sp catalog. A subsequent search upon the optical-RGB frames and redshift catalogues allowed the finding of the optical counterparts. As expected, these are blue, irregular galaxies, fainter than the limit defining the B-Sp sample.

Our strategy to search for HI emitting galaxies includes a conservative detection threshold above 6 times the rms, delivering 10, 58, 38 HI-detections in A85, A496, A2670, respectively. A few HI objects are just marginally resolved by the VLA primary beam: two in A85, six in A496, eleven in A2670. All maps and velocity fields are available as online material. We used the HI mass detection limits given in Table 3 to ensure that the sample of bright spirals (Sect. 2.5) is potentially detected with this survey. Obviously, more massive spirals have higher chances to be detected than less massive ones. Therefore, we inspect the performance of our survey detecting galaxies with different stellar masses. We displayed our HI mass detection threshold onto a M_{HI} vs M_* plot (not shown in this work). We added the scaling relation obtained by Dénes et al. (2014) and we found that normal galaxies can be effectively detected down to $\log(M_*/M_\odot) = 9.0$. The deeper data cubes in A496 pushed this limit down to $\log(M_*/M_\odot) = 8.7$. This confirms that our full sample of B-Sp can be detected with the present survey under unperturbed conditions.

Tables A1, A2 and A3 give the main optical and HI-parameters of the detected galaxies in A85, A496, A2670 respectively. The lists of non detected spirals are given in Tables B1, B2, B3 for the same clusters. Five HI detections in A496 could not be properly measured as we did not recover their full emission; this is due to limited velocity coverage of the corresponding data cube. We consider these galaxies as HI detections because the recovered emission has large S/N; they are indicated with black squares in Figs. 2 and 3.

In Tables A1, A2, A3, the first five columns give names, coordinates and morphological type; these data are taken from the literature (NED⁵ and HyperLEDA⁶). Column 6 and 7 give optical magnitudes and $(g - r)$ colors obtained from CFHT and from Pan-STARRS images. In Column (8) we provide the stellar masses obtained from our M_r magnitudes. Columns (9) and (10) give the optical and HI velocities, the latter in heliocentric frame. We consider the value of the central channel displaying emission as the HI velocity. We give the HI velocity width in Column (11) defined by the full range of channels containing emission; this constitutes a proxy for W_{20} . The HI mass (Column 12) in solar masses is calculated by using the equation:

$$\left[\frac{M_{\text{HI}}}{M_\odot} \right] = 2.36 \times 10^5 \cdot \left[\frac{D_c}{\text{Mpc}} \right]^2 \cdot \left[\frac{S_{\text{HI}}}{\text{Jy km s}^{-1}} \right] \quad (1)$$

where we use the corresponding comoving distance (D_c) for all the members of the same system. The uncertainty for M_{HI} is systematically $\leq 10\%$, derived from the computed error on the total flux S_{HI} . The HI-deficiency is estimated with the equation (Haynes & Giovanelli 1984):

$$Def_{\text{HI}} = \log(M_{\text{HI}})_{\text{exp}} - \log(M_{\text{HI}})_{\text{obs}} \quad (2)$$

⁵ <https://ned.ipac.caltech.edu/>

⁶ <http://leda.univ-lyon1.fr/>

Table 4. Different types of galaxies in the studied clusters

	Sample	A85	A496	A2670
(1)	Members	616	383	318
(2)	Memb. VLA-FoV	603	336	254
(3)	HI-det	10	58	38
(4)	B-Sp	65	46	61
(5)	B-Sp HI-det	9	29	33
(6)	B-Sp HI non-det	56	17	28
(7)	B-Sp in red seq	6	17	8
(8)	HI-det in red seq	0	11	5
(9)	HI-det abnormal	1	17	18
(10)	HI-det low mass	1	28	4
(11)	Memb. virial-region	140	203	108
(12)	B-Sp virial-region	23	20	17
(13)	HI-det virial-region	1	24	12

Given that only a reduced number of our galaxies has reliable morphological types in the literature, we computed the Def_{HI} parameter for the two cases proposed by Haynes & Giovanelli (1984), *i.e.* for early-spirals and for late-spirals. These values can be taken as lower and upper limits (Columns 13 and 14) of the deficiency parameter. Column (15) gives the projected distance to the cluster center, using the BCG position. In Column (16) we provide a code indicating four different kinds of disruptions observed in HI; this helps to define the sub-sample of HI abnormal galaxies. The codes given in this column are the following:

- *N*: galaxies with normal HI content and distribution.
- *Def*: indicates galaxies having lost more than 50% of their gas ($Def_{\text{HI}} \gtrsim 0.25$).
- *Asy*: denotes a resolved HI asymmetry, or a tail, unveiled by the HI maps.
- *Pos*: indicates an offset ≥ 20 kpc in position, between the HI and optical centroids; this limit roughly corresponds to the diameter of a typical spiral and is equivalent to $19''$, $30''$, $14''$, for A85, A496, A2670 respectively.
- *Vel*: denotes a velocity offset between the optical and HI velocities; we use three times the HI channel width to define this offset (~ 135 km s⁻¹).

Galaxies having at least one of the four criteria mentioned above are defined as HI abnormal. We used this sub-sample of perturbed objects to carry out a search for a correlation between HI-deficiency and HI-asymmetry, finding no obvious trend. However this result based on gas deficient, yet HI detected galaxies, must be taken with caution as these objects are caught at an early stripping phase. We have no information on the 2-D gas distribution of the even more stripped spirals, *i.e.* those not detected in HI. Therefore a deficiency–asymmetry correlation, developing during later gas stripping stages, should not be discarded *a priori*.

3.2 Global distribution of HI across the studied clusters

Some of our main results are displayed in Fig. 3, Fig. 4 and in Table 4. The (RA, Dec) distribution of member galaxies in the three studied clusters is shown in Fig. 3. We use the same symbols as in Fig. 2 in order to emphasize the position of the

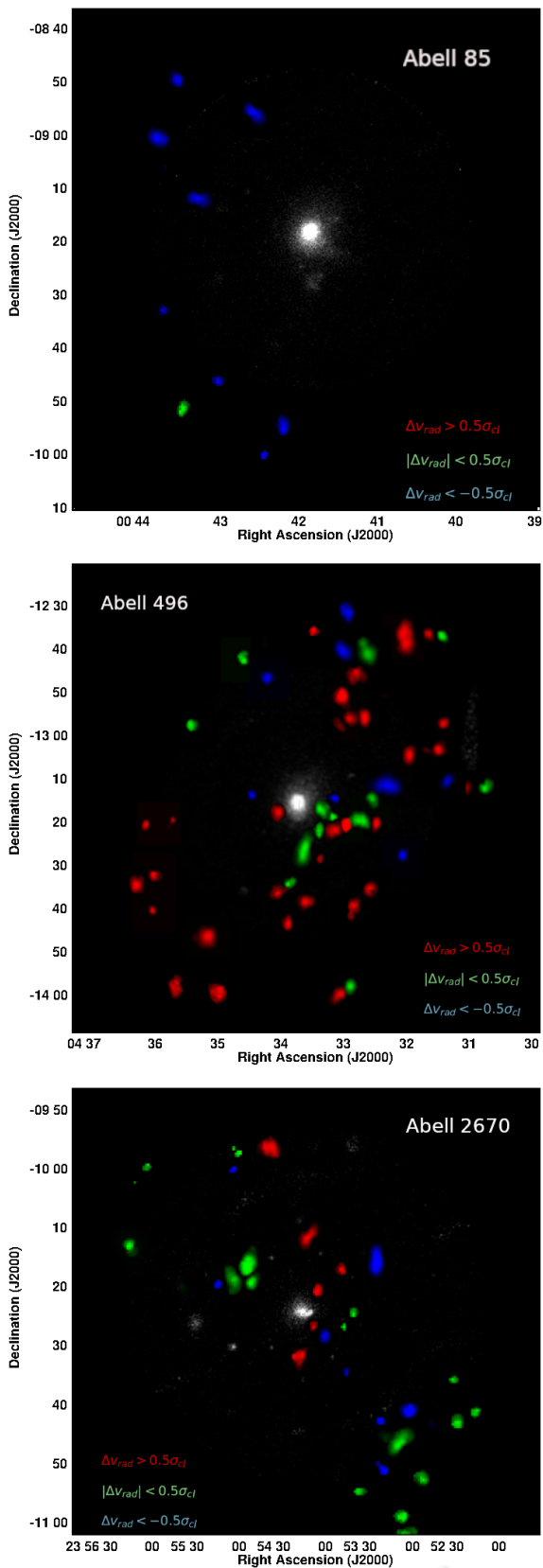


Figure 4. The distribution of HI detected galaxies in A85 (top), A496 (middle) and A2670 (bottom). These objects are separated in three slices of velocity relative to the cluster center (see text). The HI maps are enlarged by a factor of 5. The ROSAT X-ray emission is shown in grey scale.

bright spirals (blue/red circles) and the HI-detected galaxies (open blue squares/black diamonds). The total fields covered with the VLA are drawn with blue polygons and the corresponding R_{200} are indicated with red circles.

Fig. 4 shows the moment-zero HI-maps of the detected galaxies in each cluster. Galaxies are set at their proper location and are magnified by a factor of five for clarity. We use a color code in order to separate these galaxies in three radial velocity regimes: lower, similar and larger than the cluster velocity. We give statistical significance to the velocity slots by applying the same criteria as Wang et al. (2021), given as a function of the velocity dispersion of the cluster (σ_{cl}) given in Table 1: blue color for $\Delta v_{rad} < -0.5\sigma_{cl}$, green for $-0.5\sigma_{cl} < \Delta v_{rad} < 0.5\sigma_{cl}$, and red for $0.5\sigma_{cl} < \Delta v_{rad}$. The X-ray emission is shown in grey scale taking advantage of the homogeneous and large field map given by ROSAT.

Table 4 reports the total number of objects having different observational properties and lying in specific cluster regions. Data are displayed as follows: Row (1) gives the full number of cluster members, including the new members derived from the HI velocities. Row (2) provides the number of galaxies within the VLA FoV. Rows (3) and (4) give the total number of HI detections and bright spirals. Rows (5), (6), (7), give the number of B-Sp being HI detected, the B-Sp non-detected and the B-Sp lying in the red sequence, respectively. Rows (8), (9), (10), give the number of galaxies detected in HI lying in the red sequence, the HI abnormal, and those below the limit $\log(M_*/M_\odot) = 9.0$, respectively. The last three rows, (11), (12), (13), provide the number of galaxies projected within the virial region (Sect. 5.2) being: cluster members, bright spirals and HI detections, respectively. The data given in Table 4 are not well suited for a direct comparison of the clusters with each other because of their different redshifts and VLA coverage. We carry out a comparison under homogeneous conditions in Sect. 6.

• The HI in Abell 85

Fig. 3 (upper panel) shows the distribution of 616 member galaxies in A85 where the solid circles indicate the 65 B-Sp. The blue open squares and one black diamond indicate the ten HI detected objects. The cluster members (grey crosses) are rather homogeneously distributed across A85, while the B-Sp and the HI-detected galaxies show a very asymmetric distributions across the cluster. The SE zone has more bright spirals than all the other quadrants taken together; all the HI-detections are projected as well onto the SE-NE regions (Fig. 3 and Fig. 4). The gas rich galaxies are projected 1.5–3.0 Mpc away from the cluster center, while a remarkable absence of HI detections at lower radius suggests the presence of a harsh environment. This fact is independently supported by the presence of strongly perturbed galaxies (Venkatapathy et al. 2017; Ramatsoku et al. 2020; Lubert et al. 2022).

The sample of 65 B-Sp in A85 is unexpectedly high. A significant fraction of these objects are projected around the cluster core and in the transition zone between the center and the SE (Fig. 3). Six B-Sp are reaching the red sequence (red solid circles in Fig. 2) and none of them is detected in HI, indicating that they have gone through an advanced stripping process. On the contrary, all the galaxies detected

in HI show very blue colors indicating that they have not gone through any stripping phase.

The asymmetry in the distribution of HI-detections is even more striking in Fig. 4, showing that all –but one– detections are in the low velocity domain, with a narrow Δv of $\sim 15,000\text{--}15,200\text{ km s}^{-1}$ (see Table A1). Their low velocity dispersion and the large difference compared with the systemic velocity of A85 ($\sim 1,500\text{ km s}^{-1}$) suggest that they could share a common origin.

• The HI in Abell 496

The middle panel of Fig. 3 shows the distribution of 383 member galaxies in A496, with 46 B-Sp and 58 galaxies detected in HI (symbols are the same as in Fig. 2). A first remarkable difference of A496 when compared with A85 is given by the lower number of bright spirals (46 in A496, and 65 in A85) but a much larger number of HI-detections (58 in A496 for only 10 in A85; see Table 4). Interestingly, $\sim 50\%$ of the HI detected galaxies in A496 correspond to gas-rich, low mass objects which are not part of the B-Sp sample, *i.e.* their stellar mass is below $\log(M_*/M_\odot) = 9.0$. This fraction is partly explained by A496 being closer than the other studied clusters. However, we will show that some peculiarities remain after considering the observational bias due to the difference in redshift.

The distribution of HI-detected objects in A496 (Fig. 3) is striking, with many HI normal galaxies projected onto the central regions. The middle panel of Fig. 4 helps to solve the paradox: the objects with low velocity relative to the cluster (maps in green, in the velocity range $-0.5\sigma_{cl} < \Delta v_{rad} < 0.5\sigma_{cl}$) could be dominated by a movement on the plane of the sky, with circular orbits still far from the densest ICM regions (Dressler 1986). The sample of red maps projected close to the cluster core in Fig. 4 have large components of velocity along the line of sight. They must be at an early stage of infalling, accounting for their normal gas content.

Seventeen B-Sp in A496 are found in the red sequence; eleven of them still retain enough gas to be detected, some are classified as HI abnormal and are indicated with black diamonds in Fig. 2 and Fig. 3. This strongly suggests that they are under an advanced process of stripping. Most of the red spirals in A496 are projected in the NW and SE quadrants; in Sect. 6 we discuss a possible relation between their gas properties and their location within the cluster.

• The HI in Abell 2670

The bottom panel of Fig. 3 shows the distribution of 315 member galaxies in A2670, emphasising the position of 61 bright spirals and 38 HI-detections (same symbols as previous figures). From the 61 B-Sp reported in this cluster, 28 are not detected in HI, suggesting an active sweeping process. Fig. 2 shows 8 B-Sp in the red sequence, some of them retaining enough gas to be detected in HI.

Fig. 3 unveils a complex distribution of the HI detections in A2670 which are mostly projected onto the cluster core and to the SW. Most of the HI non-detected bright spirals in A2670 (solid blue/red circles without square or diamond in Fig. 3), are located near the core and to the NE. Fig. 4 shows a trend of abundant HI rich galaxies in the SW while the NE beyond $1 R_{200}$ is very poor in HI. The center shows a balance between shrunk and extended HI maps but we remind that strong projection effects might be present in this zone.

4 CLUSTER SUBSTRUCTURE ANALYSIS

In order to get a better understanding of the assembly history of the studied clusters we carried out a search for substructures based on two independent methods: the tests proposed by Dressler & Shectman (1988) and by Serna & Gerbal (1996). For the two tests we applied the compilation of member galaxies described in Sect. 2. In general we have found large coincidences with the two methods. The detected substructures are shown in Fig. 5 and they will be used, in combination with the positions of HI abnormal galaxies, as a test for pre-processing (Sect. 6).

4.1 Substructures: the Δ -test

We applied an improved version of the well known Δ -test (Dressler & Shectman 1988), which is based on the parameter- δ , defined by:

$$\delta^2 = \frac{N_{nn} + 1}{\sigma_{cl}^2} [(v_{local} - v_{cl})^2 + (\sigma_{local} - \sigma_{cl})^2] \quad (3)$$

where v_{cl} and σ_{cl} are the cluster global parameters, and v_{local} and σ_{local} are the local parameters calculated for every galaxy relative to its N_{nn} nearest neighbours. In this work we assume $N_{nn} = 10$; modifying this parameter does not change significantly our results (Bravo-Alfaro et al. 2009).

The Δ -test detects a substructure as a concentration of galaxies showing high values of the parameter- δ ; this has proven to be a reliable tracer of substructures. However, this method loses some accuracy in certain cases, for instance, when two groups at different distances from the observer are projected along the same LOS. In this case the Δ -test will produce one single overestimation of the parameter- δ , detecting only one structure. This is critical in the absence of a dominating large structure, like in bimodal/multimodal systems. In order to improve this method we introduce dividing surfaces on a 3D distribution of RA, Dec and v_{loc} . This separates the sub-groups of galaxies that share the same kinematic properties within their particular caustics, but somehow detached from the kinematics of the whole cluster. That is, we do not take into account only the parameter- δ , but also the v_{loc} and the phase-space distribution of galaxies that are candidates to be members of the substructures (more details in Caretta et al., 2022, in prep.). Values of the parameter- δ are illustrated in Fig. 5 by black circles; these circles grow with the probability of a galaxy to belong to a group. Individual values of the parameter- δ will be available upon request.

• Δ -test results in A85

We revisit the analysis of substructures of A85 (Bravo-Alfaro et al. 2009) by taking advantage that the number of redshifts for member galaxies has grown significantly in the last years (*e.g.*, Boué et al. 2008b). For the full sample of cluster members we report a velocity dispersion of $\sigma_v = 1,054\text{ km s}^{-1}$. We report the following substructures.

- The main cluster body, with 532 galaxies, has a central velocity $v = 16,650\text{ km s}^{-1}$, and $\sigma_v = 1,092\text{ km s}^{-1}$.
- The South-East (SE) substructure, with 15 members, has $v = 15,157\text{ km s}^{-1}$, and $\sigma_v = 298\text{ km s}^{-1}$.
- The *Filament group F*, with 10 objects, $v = 15,840\text{ km s}^{-1}$,

and $\sigma_v = 372 \text{ km s}^{-1}$; this and the SE substructures did not change significantly, compared with previous works, as only few new redshifts are provided for these regions.

- The Southern Blob (SB) is better defined than in previous articles; it has 38 members, $v = 16,947 \text{ km s}^{-1}$, and $\sigma_v = 282 \text{ km s}^{-1}$.

- An interesting difference compared with previous works is the C2 substructure (see Fig. 4 of Bravo-Alfaro et al. 2009) which has lost its signal because the dominant object, the jellyfish galaxy KAZ-364 (also known as JO201), lies slightly outside of the caustic contours. This galaxy is outside the velocity range of our HI cubes, so it is not included in the present analysis. Despite a velocity of $\sim 3,000 \text{ km s}^{-1}$, relative to the cluster, Bellhouse et al. (2017) reported this object as a fast, infalling cluster member being part of a small group.

- We unveiled two new low-mass substructures ($< 2\%$ of the total number of member galaxies); the first is at the South-West with 9 galaxies, $v = 16,236 \text{ km s}^{-1}$, and $\sigma_v = 183 \text{ km s}^{-1}$.

- Another new substructure lies to the NE with 12 galaxies, having $v = 16,345 \text{ km s}^{-1}$, and $\sigma_v = 300 \text{ km s}^{-1}$.

• Δ -test results in A496

We detected a main cluster body with 330 galaxies and a $\sigma_v = 674 \text{ km s}^{-1}$. We clearly unveiled one single substructure located $\sim 1^\circ$ (2.5 Mpc) NW from the cluster center, with 38 members (above 10% of the total mass), $v = 9,338 \text{ km s}^{-1}$, and $\sigma_v = 457 \text{ km s}^{-1}$ (see Fig. 5). Our HI survey covers only a small portion of that group, delivering only limited information on the cold gas associated with this structure.

• Δ -test results in A2670

We obtained the following results for A2670:

- The main cluster body emerges with 287 members, $v = 22,806 \text{ km s}^{-1}$, and $\sigma_v = 805 \text{ km s}^{-1}$.

- We unveiled two low-mass structures, the first one projected close to the center (NC, $\sim 10'$ to the north) with 7 members, $v = 22,883 \text{ km s}^{-1}$, and $\sigma_v = 20 \text{ km s}^{-1}$. This velocity suggests a merger with the main cluster body.

- The NE group lies $\sim 50'$ (4.5 Mpc), NE from the cluster center, with 14 members, $v = 23,115 \text{ km s}^{-1}$, and $\sigma_v = 424 \text{ km s}^{-1}$ (Fig. 5). This structure is just north from the VLA FoV (Fig. 3) and we do not dispose of HI information for these galaxies.

4.2 Substructures: the Serna-Gerbal test

In parallel to the Δ -test described above, we applied the Serna-Gerbal (S-G) method (Serna & Gerbal 1996) to the three clusters. This test introduces a fundamental, independent element to detect substructures: the relative potential energies of each pair of galaxies by using individual galaxy brightness as a proxy for the stellar mass. We use the r -band magnitude for this goal. In practice the S-G test requires an input catalogue of positions, velocities, magnitudes (converted to masses assuming a value of M/L), and a defined number n of galaxies needed to build a group. We used $n = 10$ as a representative value. The S-G test works hierarchically, seeking for lower level substructures within

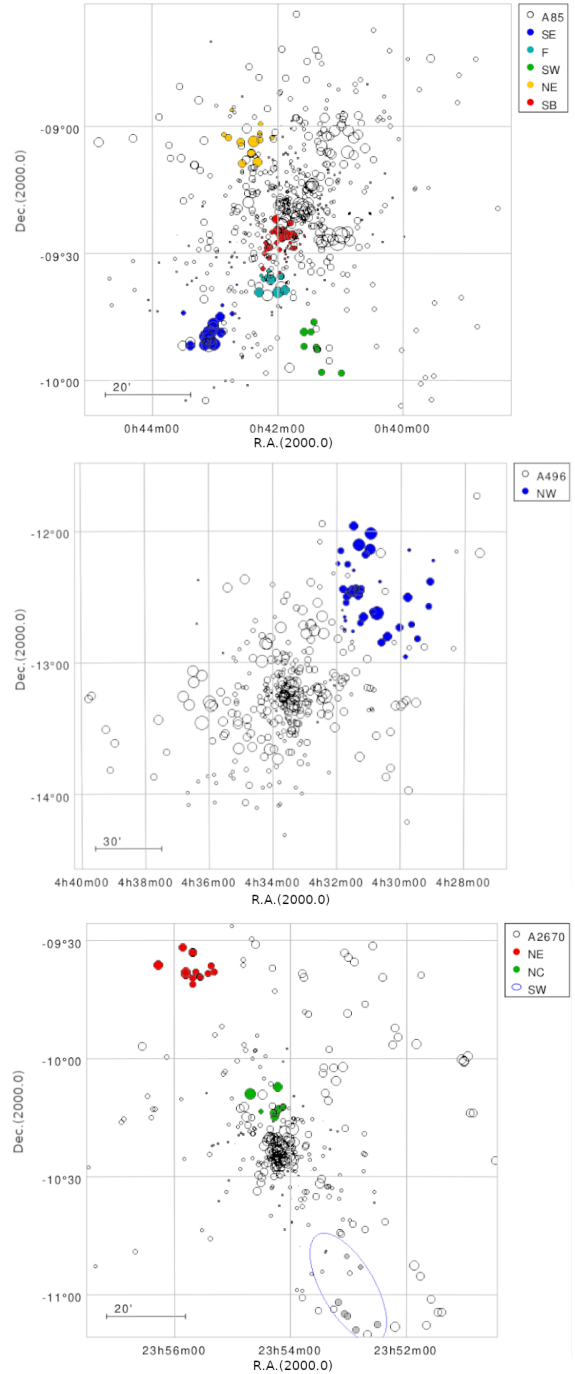


Figure 5. Substructures detected with the Δ -test. Sizes of the circles grow with the probability to belong to a substructure. Colored circles are part of the extracted groups. (Top): In A85 all but one substructure (the NE) are detected as well with the Serna-Gerbal method. (Middle): The Δ -test for A496 unveiled one large substructure to the NW. The Serna-Gerbal test found no substructures in this cluster. (Bottom): The Δ -test in A2670 detected two substructures, the NC and NE. The Serna-Gerbal test unveiled these two groups plus a third group in the SW, indicated with a blue ellipse.

a primary (more massive) detected group. This delivers an output list of galaxies belonging to each substructure and provides the mass of the corresponding group. Absolute masses of individual structures are not highly accurate, but the relative masses of the groups, normalized to the total member sample, are very reliable.

• S-G results in A85

The S-G program computed for A85 a mass of $M_{\text{tot}} = 6.51 \times 10^{14} M_{\odot}$ for the entire cluster, and a velocity dispersion of $\sigma_{\text{tot}} = 1,037 \text{ km s}^{-1}$. The S-G test detected the main cluster body (identified as #1) with 587 galaxies, a relative mass $M_1 = 0.792 M_{\text{tot}}$, and $\sigma_1 = 949 \text{ km s}^{-1}$. A secondary group (#2) is detached from the main cluster body, lying south from the center and having 21 galaxies, $M_2 = 0.079 M_{\text{tot}}$, and $\sigma_2 = 184 \text{ km s}^{-1}$. This structure is coincident with the SB group detected by the Δ -test.

In the next step we took Structure #1 as the starting point, and we unveiled two further substructures; the first one (identified as #1.1) has 144 galaxies with $M_{1.1} = 0.218 M_{\text{tot}}$, and $\sigma_{1.1} = 527 \text{ km s}^{-1}$. Some galaxies from this group account for the SE subcluster, detected as well with the Δ -test. The second substructure (#1.2) has 14 galaxies, a relative mass $M_{1.2} = 0.01 M_{\text{tot}}$, and $\sigma_{1.2} = 180 \text{ km s}^{-1}$. Finally, the group #1.1 harbors two additional substructures: the first (#1.1.1) has 74 galaxies with $M_{1.1.1} = 0.125 M_{\text{tot}}$, and $\sigma_{1.1.1} = 481 \text{ km s}^{-1}$. This group coincides in position with the minor SW structure obtained with the Δ -test. Another dozen galaxies from the structure #1.1.1 emerges as a group lying between the SB and the *Filament*, unveiling a more complex region, south of the core, than what is shown by the Δ -test. A final subgroup (#1.1.2) appears with 10 galaxies, a relative mass of $M_{1.1.2} = 0.009 M_{\text{tot}}$ and $\sigma_{1.1.2} = 173 \text{ km s}^{-1}$. This substructure matches with the *Filament* group detected with the Δ -test. With the exception of the NE group, the S-G test successfully confirmed the substructures found with the Δ -test in A85.

• S-G results in A496

We analyzed the full sample of member galaxies but we found no major substructures in A496. Even modifying the parameter n (for instance with $n=5$) we did not find significantly different results. The S-G method finds that A496 is a relaxed cluster with negligible substructuring, in agreement with previous studies (e.g. Boué et al. 2008a).

• S-G results in A2670

In the first step, the S-G test detected two groups in A2670. The largest structure (#1) has 123 galaxies with a σ_v comparable to that of the entire cluster, having $M_1 = 0.490 M_{\text{tot}}$. The second group (#2) has 10 galaxies, a mass $M_2 = 0.016 M_{\text{tot}}$, and $\sigma_{\#2} = 215 \text{ km s}^{-1}$. Group (#2) is placed $\sim 40'$ SW from the cluster center and was not detected by the Δ -test (see Fig. 5). Very interestingly, this substructure embraces the zone where several HI rich galaxies are reported (see bottom panel of Fig. 4). These objects have similar physical properties (position, velocity, gas richness), giving further support for this group to be real.

In a second run, the large structure (#1) is decomposed into two substructures (#1.1 and #1.2) having 83 and 11 galaxies respectively. The former contains

Table 5. Parameters of the ICM model

	A85	A496	A2670
r_c (kpc)	82	30	174
ρ_0 (cm^{-3})	0.0257	0.0407	0.00383
β	0.532	0.484	0.700

Notes: Parameters for A85 and A496 are taken from Chen et al. (2007). We followed Cirimele, Nesci, & Trèvese (1997) for A2670.

$M_{1.1} = 0.270 M_{\text{tot}}$, and a velocity dispersion comparable to that of the cluster. The group #1.2 contains $M_{1.2} = 0.180 M_{\text{tot}}$, and $\sigma_{1.2} = 433 \text{ km s}^{-1}$. The fact that the substructures #1 and #1.1 present high σ_v , comparable to that of the whole cluster, reduces the statistical significance for these groups, as shown by Serna & Gerbal (1996). However, part of substructure #1.1 extends from the centre to the north, coinciding with the *NC* group found with the Δ -test. The same occurs with substructure #1.2, coinciding with the *NE* group, reinforcing the existence of these two groups (Fig. 5).

The two methods, the Δ -test and the Serna-Gerbal, confirm the very complex substructure system of A85, contrasting with the very low level shown by A496. The two tests show A2670 as an intermediate case with a few, not very massive substructures.

5 RAM PRESSURE AND PHASE-SPACE DIAGRAMS

With the aim of studying the effects exerted by the ICM on the cold gas content of individual galaxies, we compute the ram-pressure stripping (RPS) profiles for the three studied clusters and compare with different values of the anchoring force (see the review by Boselli et al. (2022) for further details.) Next, we build and analyze the PPS diagrams for each cluster displaying the position of all member galaxies.

5.1 Ram pressure stripping in A85, A496, A2670

In order to estimate the RPS radial profiles we follow the theoretical definition proposed by Gumm & Gott (1972), $RPS = \rho_{\text{ICM}} \times v_{\text{rel}}^2$. Here ρ_{ICM} is the local density of the intracluster medium, and v_{rel} is the galaxy velocity relative to the ICM. We estimate the ICM density (ρ_{ICM}) as a function of the cluster radius by applying the hydrostatic-isothermal β -model of Cavaliere & Fusco-Femiano (1976), $\rho(r) = \rho_0 [1 + (r/r_c)^2]^{-3\beta/2}$. Table 5 gives the parameters of the β -model for the studied clusters: the core radius r_c , the central density ρ_0 and the β value used to calculate the density as a function of the cluster radius. The corresponding RPS profiles are shown in Figure 6 where we display three representative velocities which are multiple values of the velocity dispersion of each cluster: $0.66\sigma_{cl}$ in blue, $1.0\sigma_{cl}$ in green, and $1.5\sigma_{cl}$ in red. This adds physical meaning to the comparison of the RPS intensity among different clusters.

In order to quantify the effects produced by the RPS on individual objects it must be compared with the anchoring force per unit surface produced by the galaxy gravitational potential, given by $\Pi_{gal} = 2\pi G \Sigma_s \Sigma_g$. Here, Σ_s and Σ_g are

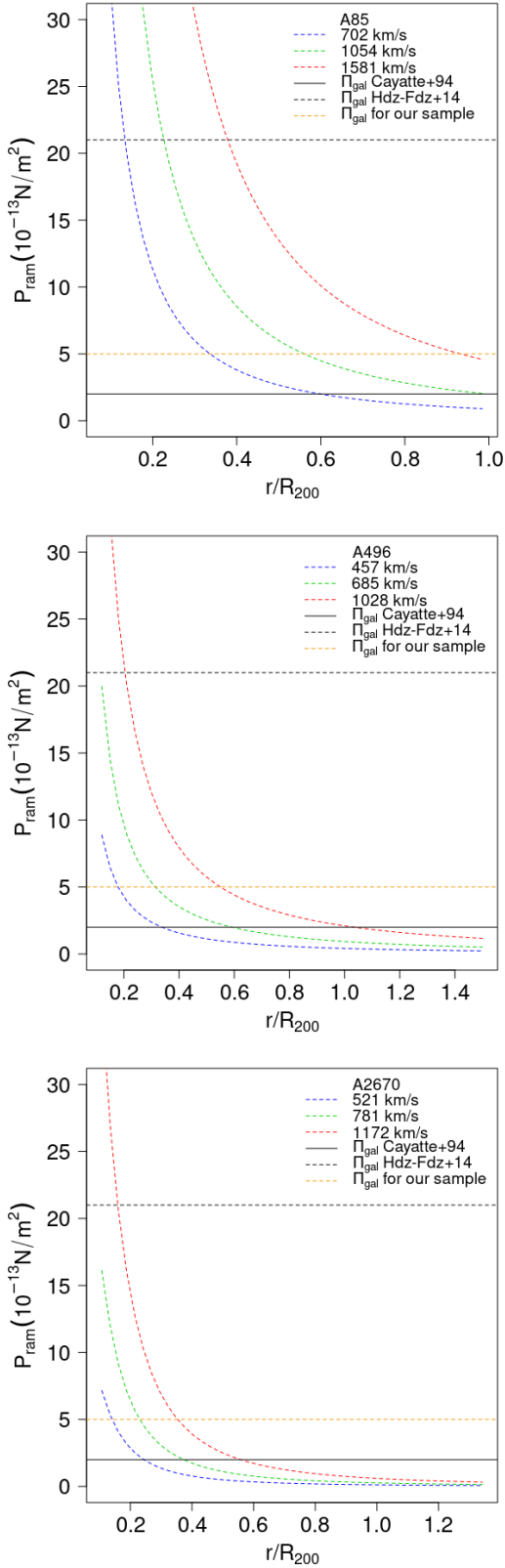


Figure 6. The RPS as a function of the cluster-centric distance. Three representative velocities relative to the ICM are displayed, taking the cluster velocity dispersion as a reference: $0.66\sigma_{cl}$ in blue; $1.0\sigma_{cl}$ in green, $1.5\sigma_{cl}$ in red. Three values of the anchoring force are shown in order to evaluate the RPS effects (see text).

the surface densities of the stellar and gaseous discs, respectively. RPS must overcome the anchoring force in order to succeed the gas stripping. Several values of Π_{gal} have been proposed, going from $2.0 \times 10^{-13} \text{ N m}^{-2}$ for spirals in Virgo (Cayatte et al. 1994), to $2.1 \times 10^{-12} \text{ N m}^{-2}$ for a Milky Way-like galaxy (Hernández-Fernández et al. 2014). One step further was made by Jaffé et al. (2018) who modelled the anchoring force as a function of the galaxy radius, the stellar mass and the gas fraction of a sample of spirals. We follow these authors in order to seek for values of Π_{gal} being representative for our sample of B-Sp.

From Fig. 2 we see that most of the B-Sp are in the range of mass between $\log(M_*/M_\odot) = 9.0$ and $\log(M_*/M_\odot) = 10.5$. No significant difference in mass is expected between our sample and that studied by Jaffé et al. (2018), so we use their Figure 5 (and Fig. 4 in Jaffé et al. 2019), which provide the anchoring force at a radius of twice the disc scale length. As we are interested in the RPS effects exerted at the external edge of spirals, we take this value as a proxy for the anchoring force acting at the outskirts of the galaxy. This strategy delivers Π_{gal} in the range from 10^{-12} to $10^{-13} \text{ N m}^{-2}$. We take the middle value $5.0 \times 10^{-13} \text{ N m}^{-2}$ as a reference for our sample of B-Sp. As a comparison, the Π_{gal} value reported by Cayatte et al. (1994) predicts very strong RPS effects, even in the low velocity and at large cluster-centric domains (see Fig. 6). The opposite is given by the value of Π_{gal} proposed by Hernández-Fernández et al. (2014). We indicate the three values of Π_{gal} in Figure 6. It is clear that the reference value $\Pi_{gal} = 5.0 \times 10^{-13} \text{ N m}^{-2}$ is more realistic for the bright spirals under study so we use it along the forthcoming analysis.

Some uncertainties are introduced though. Particularly important is the dispersion in the relation between the anchoring force and the stellar mass, with a strong dependence on the galaxy radius. In this respect Jaffé et al. (2018) have shown that the anchoring force is strongly dependent on the degree of mass concentration; this implies that low mass objects with a high central density could have a similar Π_{gal} at their center than a more massive/extended galaxy at its edge. Despite these uncertainties we will show (Sect. 6) that our reference value of Π_{gal} match reasonably well with our observations on a statistical basis.

We repeat this analysis for the low-mass galaxies, *i.e.* those in the range of stellar mass $\log(M_*/M_\odot)$ between 8.0–9.0, obtaining an upper limit for the anchoring force of $\Pi_{gal} = 10^{-13} \text{ N m}^{-2}$. Galaxies in this low regime of Π_{gal} are predicted to be easily stripped of their cold gas when they approach the virial radius. We further discuss about these objects in Sect. 6.

5.2 Phase-space diagrams and cluster accretion history

The projected phase-space (PPS) diagram of a cluster helps to distinguish virialized from infalling galaxies (*e.g.* Kent & Gunn 1982; Geller et al. 2013; Oman, Hudson, & Behroozi 2013; Jaffé et al. 2015; Rhee et al. 2017; Cortese, Catinella, & Smith 2021). We present a version of PPS where the parameters Δv and the radius are normalized by the velocity dispersion σ_{cl} , and by R_{200} , respectively. On the y-axis we display the absolute value of the peculiar velocity ($|\Delta v_{rad}|/\sigma_{cl}$). On the x-axis the projected position relative to the cluster center is normalized by R_{200} .

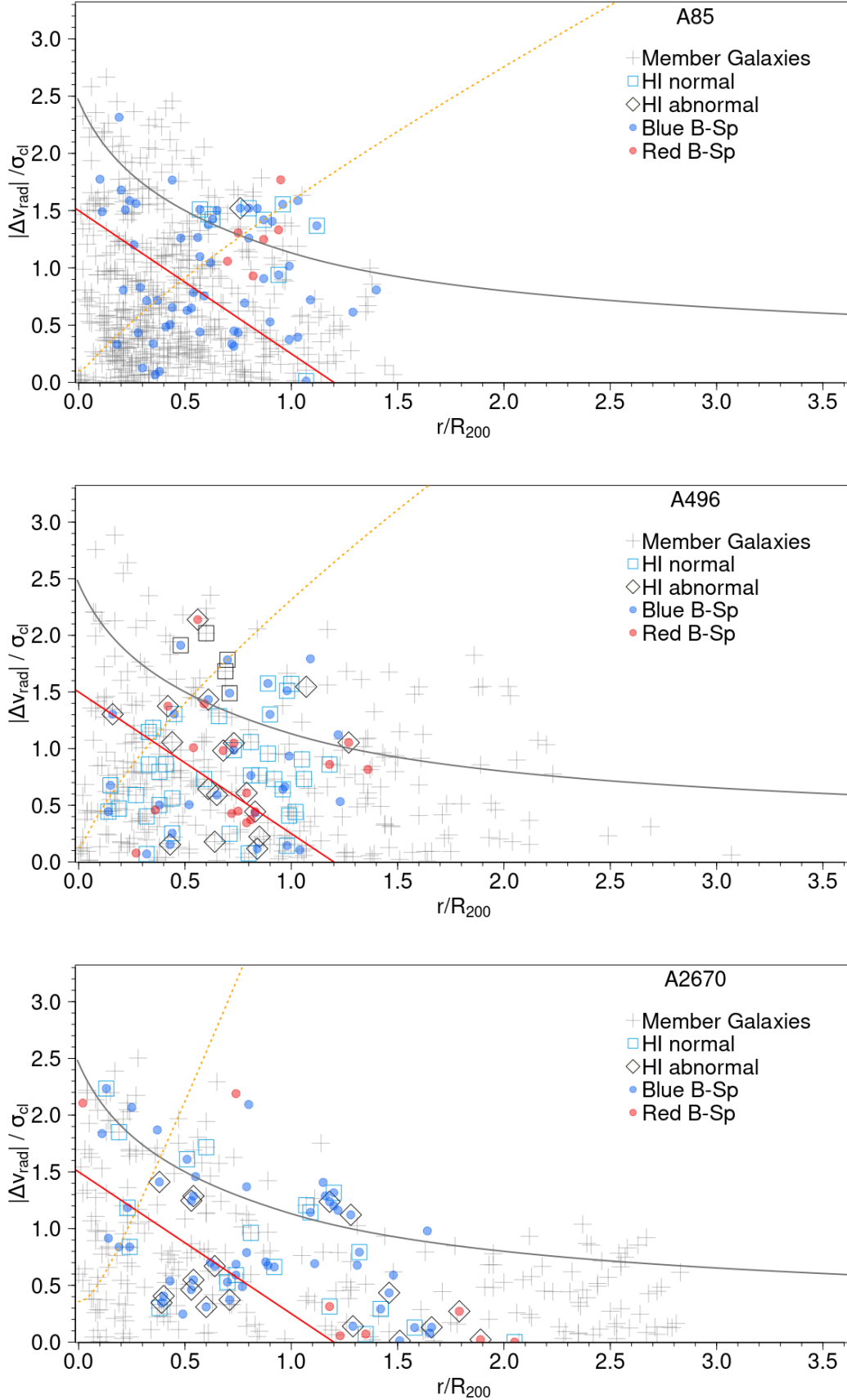


Figure 7. PPS diagrams for A85 (top), A496 (middle) and A2670 (bottom). Symbols are the same as in Figs. 2 and 3. The solid red line defines the virialized region (see text) and the solid grey line indicates the escape velocity. The dotted orange line shows the region where $P_{\text{ram}} = \Pi_{\text{gal}}$ (see Sect. 5.1).

Fig. 7 shows the PPS diagrams for A85, A496 and A2670 with the same symbols as in previous figures. The escape velocity of each cluster is shown with a solid grey line; these are more conservative than the caustics used to define the member sample and helps to obtain a better contrast between virialized and infalling galaxies (*e.g.* Jaffé et al. 2015; Wang et al. 2021). This escape velocity was estimated on the basis of a NFW halo with a concentration of $c = 6$; other values of this parameter do not change the escape velocity significantly. The orange dotted line draws the boundary where RPS equals the anchoring force, $\Pi_{gal} = 5.0 \times 10^{-13} \text{ N m}^{-2}$.

At the lower left corner of the PPS diagram we find the galaxies projected at short cluster-centric distances and having low (radial) velocities relative to the cluster. These objects are likely settled onto the cluster potential after completing –at least– one pericentric passage. This part of the diagram is identified as the *virialized zone* and we define its boundaries as follows. On the x-axis, we followed authors (*e.g.* Jaffé et al. 2015; Kopylova & Kopylov 2018) who propose that the virial radius lies in the range $1.2\text{--}1.4 R_{200}$. On the y-axis the criteria to define the virial zone is based on statistics, by considering a Gaussian distribution of velocities. We use the value of 1.5σ as a more restrictive limit (compared with 3σ) in order to avoid contamination by foreground/background galaxies. Considering these boundaries we define the virialized zone as the triangle limited by the solid red line in Fig. 7. This triangle zone is more conservative than the corresponding squared region and has been applied by authors like Jaffé et al. (2015) and Wang et al. (2021). On the opposite corner of the PPS diagrams, galaxies infalling for the first time lie in the large radii/velocity domain. After a few 10^9 yrs, equivalent to the crossing time for a typical cluster, infalling galaxies will lose kinetic energy due to dynamical friction and violent relaxation, and they will settle deep into the cluster gravitational potential.

The distribution of different types of galaxies in the PPS diagrams offer important hints on the dynamical stage of the three clusters. The top panel of Fig. 7 shows A85 behaving as a typical evolved system with a high concentration of member galaxies within the virialized zone. The escape velocity curve in this plot is lower than the one reported by Bellhouse et al. (2017); this is due to the higher mass used for A85 by these authors $M_{200} = 1.58 \times 10^{15} M_{\odot}$. We see a clear trend where, with one single exception, all B-Sp lying below the escape velocity curve are not detected in HI, suggesting that these galaxies had gone through an advanced process of gas stripping. The gas rich objects in A85 lie in the high radius, high velocity domain, indicating that they approach the cluster for the first time. Despite some similarities between A85 and other systems like A693 (*e.g.* mass, morphology and dynamical stage), their distribution of galaxies across their PPS differs significantly (Jaffé et al. 2015).

Similar to A85, A496 harbors a crowded virialized zone (medium panel of Fig. 7). This is in agreement with the advanced level of relaxation reported by different authors and with the low degree of substructuring in A496 reported in this work (Sect. 4). The striking number of HI rich galaxies lying within the virialized zone can be explained by projection effects as described in Sect. 3.2. The PPS diagram of A496 shows a slight trend of HI abnormal galaxies (black di-

amonds) and red spirals (red solid circles) being more abundant towards the virialized zone.

A2670 is dynamically young accounting for the complex distribution of galaxies in the PPS diagram and a virialized zone significantly less concentrated than in the other two systems. In this respect A2670 looks like other young clusters like Hydra (Wang et al. 2021). A number of HI detections is projected onto the virialized zone, certainly explained by projection effects. Other HI galaxies are located in the high radius ($\geq 1.5 r/R_{200}$) domain, matching with the substructure reported onto the SW in Sect. 4. Several of these detections correspond to abnormal HI galaxies (black diamonds) and to red spirals which are good candidates to be under pre-processing.

6 DISCUSSION

6.1 The HI and the effects of environment

The results described so far provide undeniable evidence on the important role played by environment in the transformation of spirals in the three studied clusters. The global cluster HI deficiency is an important parameter that correlates with the properties of galaxies in most of the nearby clusters. In this work we approach the cluster deficiency as the ratio of high HI deficient B-Sp (*i.e.* those not detected in HI) normalized by the total number of B-Sp found within each system. Cluster deficiencies calculated in this way are: 0.86, 0.37, 0.46, for A85, A496, A2670, respectively. A85 appears as an extreme case of HI deficiency and, since it is the most massive of the three studied systems, this result matches the model prediction of more massive halos producing larger gas loss (*e.g.* Donnari et al. 2021).

Next we discuss our results in the frame of four milestone results and predictions on galaxy evolution in clusters which are based on observations and on theoretical models: (1) The dependency of individual galaxy properties (like gas content and SF quenching) on the cluster-centric distance. (2) The commonly accepted role played by RPS in galaxy transformation, at least in the inner cluster regions. (3) The pre-processing of galaxies at large cluster-centric radii is thought to be responsible for the transformation of large fractions of galaxies. (4) Models of galaxy evolution predict the transformation (quenching and gas sweeping) of large fractions of satellite galaxies previous to their infalling (we refer to the following works and references therein, Peng et al. 2010; Rhee et al. 2017; Jung et al. 2018; Roberts et al. 2019; Cortese, Catinella, & Smith 2021; Donnari et al. 2021; Healy et al. 2021; Boselli et al. 2022).

We explore how the three studied clusters fit within these predictions taking into account the results described in the previous sections. With this aim we use our sample of B-Sp as test particles for environment effects. As a first approach we consider that a normal HI content *plus* a blue color constitute an indicator of a non-quenched galaxy. As mentioned previously, optical colours are not the most accurate tracers for quenching but they are often used as an alternative, distinguishing active from non-active galaxies, for instance in statistical studies as the present one. In the following discussion we take our sample of B-Sp as analogues of

the *satellite* galaxies defined in cosmological simulations. We observe that none of the B-Sp dominates any of the groups reported in Sect. 4, giving support to this approach. Current models (*e.g.* Xie et al. 2020) predict that evolution of low mass galaxies, those having $\log(M_*/M_\odot) < 10.3$ (matching the range of our B-Sp) is dominated by environmental effects. Above this threshold AGN feedback is expected to drive the galaxy quenching.

6.2 Global properties of the studied clusters

Here we compare some physical properties of the studied clusters with each other. In order to avoid part of the observational bias we focus on the inner regions, more specifically on the largest physical radius being observed with the VLA in the three systems. Based on this criteria we take the conservative value of $1R_{200}$ as comparison radius. Obviously, some bias remain due to different cluster distances which has an effect on the population of HI detected galaxies. For instance, typical HI masses reported in A85 and A2670 approach $8 \times 10^9 M_\odot$, while in A496 this value is $\sim 2 \times 10^9 M_\odot$. As a consequence, in this last cluster we report more HI galaxies in the low mass regime (Sect. 3). Nonetheless, some peculiarities described below remain even after considering this observational bias. Table 6 resumes the data corresponding to $1R_{200}$ for the three clusters.

- **A85:** This stands out as a very HI deficient system. The HI detections represent a fraction of 0.016 of the member galaxies within $1R_{200}$ (Table 6). The majority of the B-Sp not detected in HI (Fig. 7) gather towards the virial zone of the PPS diagram. This cluster shows the expected cluster-centric distribution of gas-rich/gas-poor spirals. The strongest ICM effects in A85, compared with A496 and A2670, are supported by two results given in Table 6 within $1R_{200}$: (a) the low fraction of HI detected galaxies relative to the member objects (0.01, 0.19, 0.11, in A85, A496, A2670 respectively); and (b) the fraction of B-Sp not detected in HI, relative to the B-Sp reported within the same region (0.88, 0.31, 0.51, in A85, A496, A2670 respectively). These numbers do not correlate with redshift so we discard any observational bias as responsible for this result.

These effects are well explained by RPS. We showed (Sect. 5.1) that this mechanism might exceed the anchoring force up to a radius close to $0.6r/R_{200}$ for typical (1σ) velocities, and up to $0.9r/R_{200}$ for faster infallers (1.5σ ; see Fig. 6). As a matter of fact, the central regions of A85 could be an extreme case even compared with Coma, where a number of gas deficient spirals are still detected within 1 Mpc, with similar HI mass limit detection than the present work (Bravo-Alfaro et al. 2000; Healy et al. 2021; Molnár et al. 2022). In A85 the only HI projected close to the center is the high-speed infalling jellyfish JO201, which shows signs of strong ram pressure stripping (Ramatsoku et al. 2020; Luber et al. 2022).

In parallel to RPS, we inspect the role played by pre-processing and by the shocked interface between A85 and the SE-group, in the transformation of infalling spirals. A large majority of the B-Sp which are not detected in HI are located in the SE quadrant, where the shocked interface is found. The complexity of this region is consistent with the presence of two groups (the South Blob and the Filament

groups) in addition to the SE subcluster itself (Fig. 5). Another jellyfish galaxy (JO200) is located in this zone being so deeply stripped that it was not detected in HI down to a mass limit of $9 \times 10^8 M_\odot$ (A85[DFL98]286 in Table B1). Venkatapathy et al. (2017) already proposed this galaxy to be in a more advanced stage of transformation than JO201.

A remaining number of HI non-detected B-Sp galaxies lies in the NW quadrant of A85 (Fig. 3). These objects are seen slightly beyond the escape velocity curve of the PPS of Fig. 7. No substructures are reported in that zone; therefore we favor the backsplash hypothesis (Gill, Knebe, & Gibson 2005; Hirschmann et al. 2014). This suggests that these galaxies had entered A85 from the SE and now we see them projected to the NW. Timescales for RPS quenching (~ 1 Gyr) and for cluster crossing (~ 3 Gyr) are in good agreement. Considering that morphology transformation, disregarding the responsible mechanism, takes longer timescales (~ 10 Gyr), backsplash is a plausible explanation for the spiral morphology and their location within the cluster (Boselli & Gavazzi 2006, 2014; Cortese, Catinella, & Smith 2021).

As a first approach to quantify pre-processing in A85 we obtained the number of HI perturbed galaxies, and those non-detected, within each of the groups reported in Sect. 4. We obtained the following numbers: SB:3, Filament: 4, SE: 4, SW: 0, NE: 1. This suggests that pre-processing could be at work within the groups located SE of A85. However it is difficult to separate pre-processing from the effects of the interface shocking region. The later covers very well the zone where the B-Sp not detected in HI are found.

The sample of blue, HI normal galaxies in A85 projected between 1.5 Mpc and 3.0 Mpc east of the cluster center raises some unanswered questions. They are confirmed as cluster members and, being in the stellar mass range $\log(M_*/M_\odot)$ between 9.0 and 10.0, these objects are predicted to have high probability to be quenched before their complete infall onto a massive cluster like A85 (*e.g.* Bahé et al. 2019). For instance, Xie et al. (2020) estimates that $\sim 60\%$ of galaxies would be quenched in the mass range given above and halos (clusters) with masses above $\log(M_{halo}/M_\odot) = 14.0$, which is the case for this cluster.

In any case the gas rich galaxies in A85 seem to be part of a continuous flow of newcomers occurring during several Gyr. This scenario is supported by the fact that A85 is part of the supercluster MSCC-039 which includes eleven systems (Chow-Martínez et al. 2014). The large scale structure joining A85 with its neighbors, in particular A117A, projected at ~ 12 Mpc SE of A85 (C. Caretta 2021, priv. comm.), could be responsible for the feeding of fresh HI galaxies and with the presence of the SE subcluster.

- **A496:** This cluster constitutes a puzzle not only compared with the two other systems under study but also relative to the low-*z* clusters previously imaged in HI. On one hand A496 is confirmed as a relaxed system and, in agreement with this, it is very concentrated. The PPS of Fig. 7 shows that more than 50% of member galaxies lie within the virialized zone. However, A496 presents some features in apparent contradiction with an evolved system. First, the high number of HI detections (58) constitutes 17% of the member galaxies within the VLA FoV (this is below 2% in A85; see Table 4). Even if we compensate for A496 being closer than the other two systems the trend clearly persists. Another

paradox is the absence of the expected cluster-centric distribution of HI galaxies. This is observed in clusters like Coma and A85, comparable to A496 in dynamical stage. Figs. 3 and 4 clearly show the lack of correlation. As mentioned before, particularly strong projection effects should explain the HI-rich galaxies projected onto the cluster core. This scenario fits with active ram-pressure stripping in this cluster. Our estimations predict that RPS surpass the anchoring force at $\sim 0.4 r/R_{200}$ for typical 1σ velocities, and up to $0.6 r/R_{200}$ for velocities of 1.5σ (Fig. 6). This implies that HI normal spirals are hardly expected near the cluster core.

Taking the full sample of B-Sp as test particles for environment effects we find that 37% of them have lost a large fraction of gas and were not detected in HI (Table 4). Furthermore, among the HI detected B-Sp a number of them are reported as abnormal (Table A2). If we consider the color index, one third of the B-Sp in A496 are located in the red sequence. All these results clearly indicate an important degree of spiral transformation in this cluster.

Another intriguing result in A496 is the large number of HI detected galaxies with masses below $\log(M_*/M_\odot)=9.0$, some of them having HI mass $\geq 3 \times 10^9 M_\odot$ (see Table A2). In similar clusters, like Hydra, the average HI mass for the same range of stellar mass is significantly lower, below $10^9 M_\odot$ (Wang et al. 2021). Even considering the closer distance of A496 (the nearer the cluster, larger the fraction of low-mass HI detected objects) we expected similar galaxies to be found in A85 and A2670. Taking into account our HI detection limits and by scaling the corresponding HI flux to the distance of A85 and A2670, our survey would be capable to detect such gas-rich galaxies with stellar masses around $\log(M_*/M_\odot)=8.5$. However these objects are absent, more conspicuously in A85.

The low-mass, gas-rich and very blue galaxies in A496, are very likely in a pre-quenching phase. These objects deserve a more detailed study; current models predict strong pre-processing and a significant quenching fraction, going up to 80% for $\log(M_*/M_\odot) = 9.0$, at $z = 0$ (Donnari et al. 2021). In a forthcoming paper we will try to determine, statistically, how close to a massive halo these low-mass galaxies last before extinguishing. This could help to restrict theoretical models.

Beside the projection effects, the full distribution of HI galaxies in A496 (Fig. 3) deserves a closer look. The NE quadrant is almost empty of HI objects. In the south and south-east regions, all the HI detections belong to the high velocity domain (red maps in Fig. 4), suggesting a common origin. Finally the north-west is the richest zone of both, HI detections and member galaxies. This could be associated with the only substructure found in this cluster (Sect. 4). Concerning pre-processing, the very low degree of substructures suggest that this mechanism is not playing a major role transforming infalling galaxies in A496. Instead, the cluster environment seems to dominate the processing of spirals.

We explored the surrounding large scale structure of A496 in order to better understand the replenishment of gas-rich galaxies. We analyzed 6dF Survey data within an area of 12 degrees around A496; the center of this cluster is indicated with a black solid circle in Fig. 8. We applied a galaxy request restricted to the redshift range of $0.0255 - 0.0407$ ($7552 - 11962 \text{ km s}^{-1}$), corresponding to the 3σ interval of A496. The output of 498 galaxies is displayed

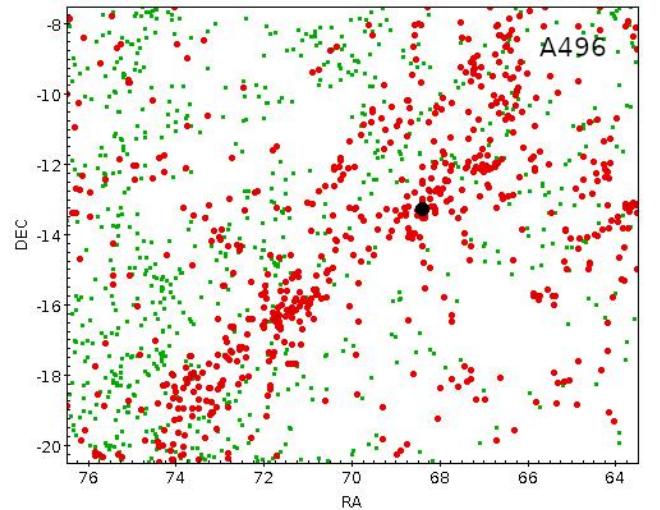


Figure 8. 6dF galaxies (green dots) found within a square of 12° of side around A496 (black diamond). Red dots indicate the 498 galaxies having velocities within the 3σ interval around A496.

in the same figure. This plot shows in green the positions of all the galaxies found in 6dF while the objects in red correspond to the selected redshift interval. Important galaxy concentrations are clearly seen, drawing a filament in the NW-SE direction, having redshifts of 0.037 and 0.038 (the redshift of A496 is 0.033). The nearest structure to A496 lies to the NW and could be at the origin of the large number of gas-rich objects in the NW zone of A496 and the substructure reported in the same region (Fig. 5). Other observational evidences support this filament of large scale structure, like the X-ray cluster MCXC J0445.1-1551, SE from A496. This system was not identified originally by Abell and is found at RA=71.5, Dec=-16, centered on the cD galaxy NGC 1650. These filaments account for the observed replenishment of gas rich galaxies, in particular from the NW.

- **A2670:** This system is dynamically younger than the other studied clusters so the high fraction of B-Sp within the VLA FoV (24%, see Table 4) is not unexpected. The fraction of B-Sp within $1 R_{200}$ is larger than in the other two systems (Table 6). However, opposite to other young clusters like Virgo (Chung et al. 2009), Hydra (Wang et al. 2021) and Abell 963 (Jaffé et al. 2015), the correlation between HI deficiency and cluster-centric radius is not seen in A2670. This is due to the large number of HI rich galaxies projected onto the cluster core (Figs. 3 and 4) which are located into the virialized zone of the cluster (Fig. 7). Our estimations of RPS in A2670 predict significant environment effects, even if less intense than in A496 and A85. In A2670, RPS is expected to dominate within $r/R_{200} \leq 0.3$, for relative velocities of $\sim 1.0\sigma$, and within a radius of $r/R_{200} \leq 0.4$, for higher velocities $\sim 1.5\sigma$ (Fig. 6). Therefore most of the HI detections projected in the very central region of A2670 are explained by projection effects, either being fast infallers along the line of sight or objects with non-radial orbits.

We use the B-Sp properties to investigate the strength

Table 6. Different types of galaxies within $1 R_{200}$: comparing the inner regions of A85, A496, A2670.

Galaxies (1)	Normalized by: (2)	A85		A496		A2670	
		# (3)	(fract.) (4)	# (5)	(fract.) (6)	# (7)	(fract.) (8)
Members		574		271		195	
Hr-det	Members	8	0.01	52	0.19	21	0.11
B-Sp	Members	58	0.10	39	0.14	35	0.18
B-Sp Hr-det	B-Sp	7	0.12	27	0.69	17	0.49
B-Sp HI non-det	B-Sp	51	0.88	12	0.31	18	0.51
B-Sp in red seq	B-Sp	6	0.10	14	0.36	2	0.06
Hr-det in red seq	Hr-det	0	0.00	7	0.13	0	0.00
Hr-det abnormal	Hr-det	1	0.13	15	0.29	10	0.48
Low mass Hr-det	Hr-det	1	0.13	21	0.40	3	0.14

Notes:

- All objects mentioned in Columns 1 and 2 are restricted to $1 R_{200}$.
- The numbers of galaxies mentioned in Column 1 are given in columns 3 (A85), 5 (A496), 7 (A2670).
- Column 2 indicates the sample used to normalize the number of galaxies referred in Column 1.
- The fractions "*Column (1) / Column (2)*" are given in Columns 4 (A85), 6 (A496), 8 (A2670).

of the environment effects in A2670. Fig. 2 shows that a number of B-Sp have reached the red sequence; five of them retain enough gas to be detected in HI. Interestingly, almost half of the HI detected galaxies are classified as abnormal (Table 4) confirming a rather harsh cluster environment. The fraction of HI abnormal objects within $1 R_{200}$ is much larger in A2670 (0.48) than the other two clusters. We quantify the importance of pre-processing in A2670 by contrasting the positions of the HI perturbed B-Sp with the substructures reported in Sect. 4. We found only two of such galaxies in the north-center (NC) group and four in the SW, including 3 HI abnormal and one non-detected object. The SW region seems to be the only zone of this cluster where pre-processing is at work.

The elongated morphology of A2670, following a NE-SW axis, is confirmed by the distribution of member galaxies in Fig. 3. The global positions of HI detections help to trace the accretion history of A2670. When we focus beyond $1.0 R_{200}$, a strong asymmetry is seen between the very HI rich south-west and the HI poor north-east region (Fig. 4). This strongly suggest the former as the preferred direction of infalling spiral galaxies.

6.3 The evolutionary stage of the bright spirals: a three-cluster composite view

In order to explore the global behavior of the large sample of bright spirals (B-Sp) collected in this work we create a composite cluster constituted by the three studied systems. The left panel of Fig. 9 shows the distribution, on the plane of the sky, of all member objects and all the bright spirals (we use the same symbols than in previous plots). The right panel of Fig. 9 shows the PPS diagram of the composite cluster. In order to properly display the three systems in a single plot we normalize the galaxy cluster-centric distance by the corresponding R_{200} . The relative velocities are normalized by the corresponding cluster velocity dispersion σ_{cl} (see Luber et al. 2022).

We study the behaviour of the B-Sp across the composite cluster by looking for trends between their distribution and their HI properties. We split the full catalog of B-Sp in two sub-samples named: *normal* B-Sp and *disturbed* B-Sp. The former is constituted by those HI detected B-Sp, displaying normal distribution and gas content. The sub-sample of *disturbed* B-Sp includes those being HI abnormal *plus* those HI non-detected. Defined in this way, the disturbed sub-sample includes galaxies undergoing strong degrees of transformation. Next we estimate the mean projected distances for each sub-sample and we compare them. We use units of r/R_{200} , obtaining the following results:

normal B-Sp: $\mu_1=0.63$;
disturbed B-Sp: $\mu_2=0.56$.

This confirms the expected scenario where HI disturbed spirals are located, on average, closer to the cluster center than HI normal ones. The difference between means is, however, not found to be significant enough ($1 - p \lesssim 90\%$) by the Welch's t-test. As we next show, this is most likely due to the heterogeneous trends seen in the individual clusters. In order to quantify such trends we contrasted the average distances of the same sub-samples within each system:

A85: normal B-Sp: $\mu_1=0.86$ vs. disturbed B-Sp: $\mu_2=0.59$.
A496: normal B-Sp: $\mu_1=0.66$ vs. disturbed B-Sp: $\mu_2=0.75$.
A2670: normal B-Sp: $\mu_1=0.96$ vs. disturbed B-Sp: $\mu_2=0.85$

This confirms, in A85, the very strong trend where disturbed B-Sp lay at lower cluster-centric radius (confidence value $> 99\%$). Oppositely, A496 has a very atypical behaviour with an inverse trend of normal B-Sp located, in average, at lower radius than their disturbed counterparts. Despite the projection effects cited above, such a trend has never been observed in other clusters. A2670 is an intermediate case where the difference between μ_1 and μ_2 has low statistical significance. Other statistical methods produce similar results, for instance the Two-sample test for the mean, considering the one-tail case of the z-Test.

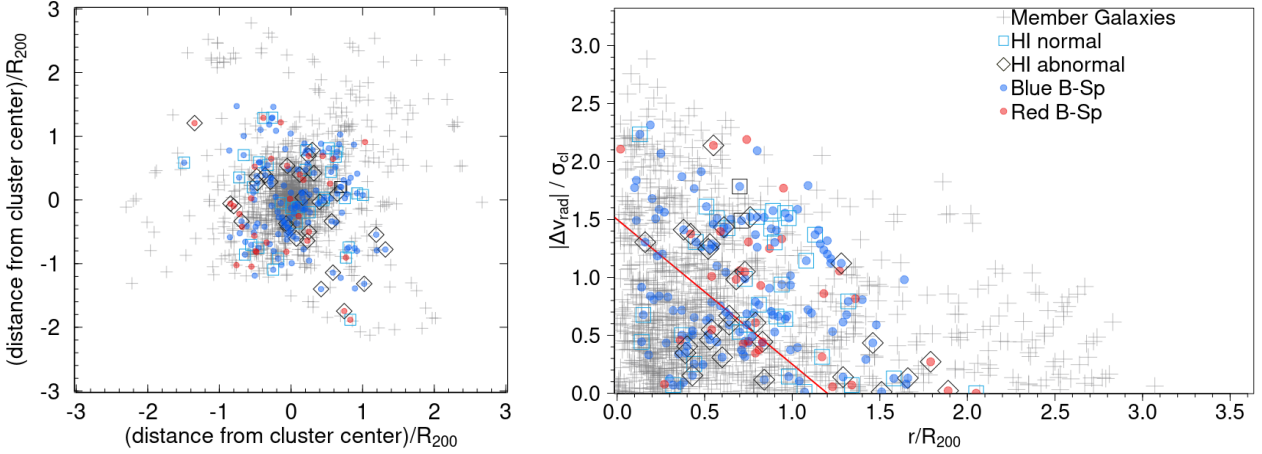


Figure 9. Composite plots of three clusters showing the member galaxies (grey crosses), highlighting the bright spirals; blue/red spirals are shown with solid circles; HI detections are given with squares and diamonds, indicating normal and abnormal objects, respectively. Left panel: the projected position on the sky, normalizing cluster-centric distances by R_{200} . Right panel: positions of galaxies in the phase space diagram. The red line delimits the virialized zone as defined in Fig. 7.

7 SUMMARY AND CONCLUSIONS

This paper is devoted to study galaxy evolution and environment effects occurring at the core and outskirts of three nearby Abell clusters: A85/A496/A2670. We analyzed the transformation of spirals as a function of their local environment by studying different clusters lying at roughly the same cosmological epoch. This work is based on a blind, VLA HI-imaging survey, with data cubes covering a volume that extends beyond one virial radius and more than three times the velocity dispersion of each cluster. Our main results and conclusions can be summarized as follows.

- We report HI parameters for 10, 58, and 38 galaxies in A85, A496, and A2670, respectively, as well as an atlas of the corresponding HI maps and velocity fields. We defined a complete sample of bright spirals with masses above $\log(M_*/M_\odot) = 9.0$ and we used them as test particles for environment effects. This sample helped as well to obtain a catalog of the spirals not detected in HI and to trace the accretion history of the parent clusters.
- We report further evidence for cluster environment playing an active role in transforming spirals, both in their HI content and in their color. We measured the global HI deficiency of the three clusters, finding a very high value (85%) for A85, and less conspicuous deficiencies for A496 and A2670. The expected cluster-centric distribution of HI rich/poor galaxies is only observed in A85. The other two systems show a very complex distribution of their HI, with a high fraction of gas-rich objects lying within the virialized zone. Strong projection effects must be responsible.
- We report a number of bright spirals that have moved into the red sequence in the three clusters. The majority of these objects are HI disturbed. This sample of red spirals constitutes additional evidence for systematic transformation from normal, blue spirals, into gas poor, passive objects.
- We traced ram-pressure stripping profiles in order to

measure the strength of environment effects due to the intracluster medium. We find that RPS accounts for the disrupted/stripped galaxies in the central regions of the three studied clusters. The inner 1.5 Mpc (roughly one virial radius) of A85 appears to be particularly harsh, only compared with clusters like Coma.

- Our substructure analysis confirms A85 as a complex system with several minor groups and a major SE subcluster merging with the main cluster body. We report two new groups in A85, one to the SW and a second to the NE. In A496 we unveiled a large group NW of the cluster center. We revisited the surrounding large scale structure of A496 and we detected a filament running NW-SE. A2670 is an intermediate case between the two other studied clusters, having three minor groups running along the NE-SW axis. The distributions of HI rich/poor galaxies in the three clusters reveal the following (preferred) directions of galaxy infalling: the SE for A85, NW for A496, and SW for A2670.
- We explored the relevance of pre-processing by measuring the number of HI disturbed galaxies within each of the reported substructures. In A85 we found an important number of such disturbed objects, SE from the cluster center. They could be produced by a shocked interface due to a cluster-subcluster merger process and/or by pre-processing. The other two clusters show no evidence for strong pre-processing with the exception of the SW group of A2670. Our results suggest that the effects of the global cluster environment are equally (or even more) important than pre-processing in the transformation of spiral galaxies.
- The systematic transformation of spirals in the studied clusters cannot be associated to one single parameter of the parent system. Therefore, in addition to the cluster mass and L_X , the dynamical stage and the feeding of new spirals from the large scale structure help to explain the observed properties of the spiral population and their degree of transformation.

ACKNOWLEDGEMENTS

The authors thank the anonymous referee for her/his helpful comments which helped to improve this paper. M.M.L.G., H.B.A. and C.A.C. acknowledge funding from CONACyT and DAIP. H.B.A. also thanks *Institut d'Astrophysique de Paris* for its support during his working visits. We acknowledge Y. Venkatapathy for his help enlarging the redshift catalogues used in this work. F.D. acknowledges continuous support from CNES since 2002. Y.J. acknowledges financial support from FONDECYT Iniciación 2018 No. 11180558 and ANID BASAL Project FB210003.

Data availability.

Data available on request.

REFERENCES

- Arnouts S., Walcher C. J., Le Fèvre O., Zamorani G., Ilbert O., Le Brun V., Pozzetti L., et al., 2007, *A&A*, 476, 137
- Bahé Y. M., McCarthy I. G., Balogh M. L., Font A. S., 2013, *MNRAS*, 430, 3017
- Bahé Y. M., Schaye J., Barnes D. J., Dalla Vecchia C., Kay S. T., Bower R. G., Hoekstra H., et al., 2019, *MNRAS*, 485, 2287
- Balogh M., Eke V., Miller C., Lewis I., Bower R., Couch W., Nichol R., et al., 2004, *MNRAS*, 348, 1355
- Barsanti S., Owers M. S., Brough S., Davies L. J. M., Driver S. P., Gunawardhana M. L. P., Holwerda B. W., et al., 2018, *ApJ*, 857, 71
- Barnes J. E., Hernquist L., 1996, *ApJ*, 471, 115
- Barway S., Kembhavi A., Wadadekar Y., Ravikumar C. D., Mayya Y. D., 2007, *ApJ*, 661, L37
- Bellhouse C., Jaffé Y. L., Hau G. K. T., McGee S. L., Poggianti B. M., Moretti A., Gullieuszik M., et al., 2017, *ApJ*, 844, 49
- Boselli A., Gavazzi G., 2006, *PASP*, 118, 517
- Boselli A., Gavazzi G., 2014, *A&ARv*, 22, 74
- Boselli A., Lupi, A., Epinat, B., et al. 2021, *A&A*, 646, 139
- Boselli A., Fossati, M., Sun, M. 2022, *A&ARv*, 30, 3
- Boué G., Adami C., Durret F., Mamon G. A., Cayatte V., 2008, *A&A*, 479, 335
- Boué G., Durret F., Adami C., Mamon G. A., Ilbert O., Cayatte V., 2008, *A&A*, 489, 11
- Bravo-Alfaro H., Cayatte V., van Gorkom J. H., Balkowski C., 2000, *AJ*, 119, 580
- Bravo-Alfaro H., Cayatte V., van Gorkom J. H., Balkowski C., 2001, *A&A*, 379, 347
- Bravo-Alfaro H., Caretta C. A., Lobo C., Durret F., Scott T., 2009, *A&A*, 495, 379
- Briggs D. S., 1995, *AAS*
- Butcher H., Oemler A., 1978, *ApJ*, 219, 18
- Byrd G., Valtonen M., 1990, *ApJ*, 350, 89
- Bryan G. L., Norman M. L., 1998, *ApJ*, 495, 80
- Cavaliere A., & Fusco-Femiano R., 1976, *A&A*, 49, 137
- Cayatte V., van Gorkom J. H., Balkowski C., Kotanyi C., 1990, *AJ*, 100, 604
- Cayatte V., Kotanyi C., Balkowski C., van Gorkom J. H., 1994, *AJ*, 107, 1003
- Chen Y., Reiprich T. H., Böhringer H., Ikebe Y., Zhang Y.-Y., et al., 2007, *A&A*, 466, 805
- Chow-Martínez M., Andernach H., Caretta C. A., Trejo-Alonso J. J., 2014, *MNRAS*, 445, 4073
- Chow-Martínez M. 2019. PhD Thesis, University of Guanajuato, Mexico.
- Chung A., van Gorkom J. H., Kenney J. D. P., Crowl H., Vollmer B., 2009, *AJ*, 138, 1741
- Cirimele G., Nesci R., & Trèvese D., 1997, *ApJ*, 475, 11
- Cortese L., Catinella B., Smith R., 2021, *PASA*, 38, 35
- De Lucia G., Hirschmann M., Fontanot F., 2019, *MNRAS*, 482, 5041
- Deb T., Verheijen M. A. W., Gullieuszik M., Poggianti B. M., van Gorkom J. H., Ramatsoku M., Serra P., et al., 2020, *MNRAS*, 494, 5029
- Dénes H., Kilborn V. A. & Koribalski B. S. 2014, *MNRAS*, 444, 667
- Dénes H., Kilborn V. A., Koribalski B. S., Wong O. I., 2016, *MNRAS*, 455, 1294
- Donnari M., Pillepich A., Joshi G., D., Nelson D., Genel S., Marinacci F., Rodriguez-Gomez V., et al., 2021 *MNRAS*, 500, 4004
- Dressler A., 1980, *ApJ*, 236, 351
- Dressler A., 1980, *ApJ*, 301, 35
- Dressler A., Shectman S. A., 1988, *AJ*, 95, 985
- Dressler A., Oemler A., Couch W. J., Smail I., Ellis R. S., Barger A., Butcher H., et al., 1997, *ApJ*, 490, 577
- Durret F., Forman W., Gerbal D., Jones C., Vikhlinin A., 1998, *A&A*, 335, 41
- Durret F., Felenbok P., Lobo C., Slezak E., 1999, *A&AS*, 139, 525
- Durret F., Adami C., Gerbal D., Pislari V., 2000, *A&A*, 356, 815
- Durret F., Lima Neto G. B., Forman W., 2005, *A&A*, 432, 809
- Fadda D., Biviano A., Marleau F. R., Storrie-Lombardi L. J., Durret F., 2008, *ApJ*, 672, L9
- Fasano G., Poggianti B. M., Couch W. J., Bettoni D., Kjærgaard P., Moles M., 2000, *ApJ*, 542, 673
- Fernández X., van Gorkom J. H., Hess K. M., Pisano D. J., Kreckel K., Momjian E., Popping A., et al., 2013, *ApJL*, 770, L29
- Fernández X., Gim H. B., van Gorkom J. H., Yun M. S., Momjian E., Popping A., Chomiuk L., et al., 2016, *ApJ*, 824, L1
- Finn R. A., Zaritsky D., McCarthy D. W., Poggianti B., Rudnick G., Halliday C., Milvang-Jensen B., et al., 2005, *ApJ*, 630, 206
- Flewelling, H. A., Magnier, E. A., Chambers, K. C. et al. 2020, *ApJS*, 251, 7
- Geller M. J., Diaferio A., Rines K. J., Serra A. L., 2013, *ApJ*, 764, 58
- Gill S. P. D., Knebe A., Gibson B. K., 2005, *MNRAS*, 356, 1327
- Giovanelli R., Haynes M. P., 1985, *ApJ*, 292, 404
- Giovanelli R., Haynes M. P., Kent B. R., Perillat P., Saintonge A., Brosch N., Catinella B., et al., 2005, *AJ*, 130, 2598
- Gogate A. R., Verheijen M. A. W., Deshev B. Z., van Gorkom J. H., Montero-Castaño M., van der Hulst J. M., Jaffé Y. L., et al., 2020, *MNRAS*, 496, 3531
- Goto T., Yamauchi C., Fujita Y., Okamura S., Sekiguchi M., Smail I., Bernardi M., et al., 2003, *MNRAS*, 346, 601
- Gunn J. E., Gott J. R., 1972, *ApJ*, 176, 1
- Haynes M. P., Giovanelli R., 1984, *AJ*, 89, 758
- Haynes M. P., Giovanelli R., Kent B. R., Adams E. A. K., Balonek T. J., Craig D. W., Fertig D., et al., 2018, *ApJ*, 861, 49
- Healy J., Blyth S.-L., Verheijen M. A. W., Hess K. M., Serra P., van der Hulst J. M., Jarrett T. H., et al., 2021, *A&A*, 650, A76
- Hernández-Fernández J. D., Haines C. P., Diaferio A., Iglesias-Páramo J., Mendes de Oliveira C., Vilchez J. M., 2014, *MNRAS*, 438, 2186
- Hess K. M., Lubert N. M., Fernández X., Gim H. B., van Gorkom J. H., Momjian E., Gross J., et al., 2019, *MNRAS*, 484, 2234
- Hirschmann, M., De Lucia, G., Wilman, D., et al. 2014, *MNRAS*, 444, 2938
- Hubble E., Humason M. L., 1931, *ApJ*, 74, 43
- Ichinohe, Y., Werner, N., Simionescu, A., et al. 2015, *MNRAS*, 448, 2971
- Jaffé Y. L., Poggianti B. M., Verheijen M. A. W., Deshev B. Z., van Gorkom J. H., 2013, *MNRAS*, 431, 2111
- Jaffé Y. L., Smith R., Candlish G. N., Poggianti B. M., Sheen Y.-K., Verheijen M. A. W., 2015, *MNRAS*, 448, 1715

- Jaffé Y. L., Verheijen M. A. W., Haines C. P., Yoon H., Cybulski R., Montero-Castaño M., Smith R., et al., 2016, *MNRAS*, 461, 1202
- Jaffé Y. L., Poggianti B. M., Moretti A., Gullieuszik M., Smith R., Vulcani B., Fasano G., et al., 2018, *MNRAS*, 476, 4753
- Jaffé Y. L., Poggianti B. M., Moretti A., Gullieuszik M., Smith R., Vulcani B., Fasano G., et al., 2019, *MNRAS*, 482, 3454
- Jonas J., MeerKAT Team, 2016, mks.conf, 1
- Jung S. L., Choi H., Wong O. I., Kimm T., Chung A., Yi S. K., 2018, *ApJ*, 865, 156
- Kauffmann G., White S. D. M., Heckman T. M., Ménard B., Brinchmann J., Charlot S., Tremonti C., et al., 2004, *MNRAS*, 353, 713
- Kent S. M., Gunn J. E., 1982, *AJ*, 87, 945
- Kopylova F. G., Kopylov A. I., 2018, *AstBu*, 73, 267
- Koribalski B. S., Staveley-Smith L., Westmeier T., Serra P., Spekkens K., Wong O. I., Lee-Waddell K., et al., 2020, *Ap&SS*, 365, 118
- Laganá T. F., Durret F., Lopes P. A. A., 2019, *MNRAS*, 484, 2807
- Larson R. B., Tinsley B. M., Caldwell C. N., 1980, *ApJ*, 237, 692
- Lewis I., Balogh M., De Propriis R., Couch W., Bower R., Offer A., Bland-Hawthorn J., et al., 2002, *MNRAS*, 334, 673
- Lopes P. A. A., Trevisan M., Laganá T. F., Durret F., Ribeiro A. L. B., Rembold S. B., 2018, *MNRAS*, 478, 5473
- Luber, N., Müller, A., van Gorkom, J. H. et al., 2022, *ApJ*, 927, 39
- Mahajan S., Drinkwater M. J., Driver S., Hopkins A. M., Graham A. W., Brough S., Brown M. J. I., et al., 2018, *MNRAS*, 475, 788
- Masters K. L., Mosleh M., Romer A. K., Nichol R. C., Bamford S. P., Schawinski K., Lintott C. J., et al., 2010, *MNRAS*, 405, 783
- Merritt D., 1983, *ApJ*, 264, 24
- Molnár, D. Cs., Serra, P., van der Hulst, T., et al. 2022, *A&A*, 659, A94
- Moore B., Katz N., Lake G., 1996, *ApJ*, 457, 455
- Nulsen P. E. J., 1982, *MNRAS*, 198, 1007
- Oemler A., 1974, *ApJ*, 194, 1
- Oman K. A., Hudson M. J., Behroozi P. S., 2013, *MNRAS*, 431, 2307
- Owers M.S., Allen J.T., Baldry I. et al., 2017, *MNRAS*, 468, 1824
- Paccagnella, A., Vulcani, B. Poggianti, B. M., et al. 2017, *ApJ*, 838, 148
- Paturel G., Fouque P., Bottinelli L., Gouguenheim L., 1989, *A&AS*, 80, 299
- Peng Y.-. jie ., Lilly S. J., Kovač K., Bolzonella M., Pozzetti L., Renzini A., Zamorani G., et al., 2010, *ApJ*, 721, 193
- Poggianti B. M., Aragón-Salamanca A., Zaritsky D., De Lucia G., Milvang-Jensen B., Desai V., Jablonka P., et al., 2009a, *ApJ*, 693, 112
- Poggianti B. M., Fasano G., Bettoni D., Cava A., Dressler A., Vanzella E., Varela J., et al., 2009b, *ApJ*, 697, L137
- Poggianti B. M., Moretti A., Gullieuszik M., Fritz J., Jaffé Y., Bettoni D., Fasano G., et al., 2017, *ApJ*, 844, 48
- Postman M., Geller M. J., 1984, *ApJ*, 281, 95
- Ramatsoku M., Serra P., Poggianti B. M., Moretti A., Gullieuszik M., Bettoni D., Deb T., et al., 2020, *A&A*, 640, A22
- Rhee J., Smith R., Choi H., Yi S. K., Jaffé Y., Candlish G., Sánchez-Jánssen R., 2017, *ApJ*, 843, 128
- Rhee J., Smith R., Choi H., Contini E., Jung S. L., Han S., Yin S. K., 2020, *ApJS*, 247, 45
- Roberts I. D., Parker L. C., Brown T., Joshi G. D., Hlavacek-Larrondo J., Wadsley J., 2019, *ApJ*, 873, 42
- Roediger E., Brüggem M., 2006, *MNRAS*, 369, 567
- Salerno J. M., Martínez H. J., Muriel H., Coenda V., Vulcani B., Poggianti B., Moretti A., et al., 2020, *MNRAS*, 493, 4950
- Serna A., Gerbal D., 1996, *A&A*, 309, 65
- Scott T. C., Bravo-Alfaro H., Brinks E., Caretta C. A., Cortese L., Boselli A., Hardcastle M. J., et al., 2010, *MNRAS*, 403, 1175
- Scott T. C., Brinks E., Cortese L., Boselli A., Bravo-Alfaro H., 2018, *MNRAS*, 475, 4648
- Serra A. L., Diaferio A., Murante G., Borgani, S. 2011, *MNRAS*, 412, 800
- Sheen Y.-K., Smith R., Jaffé Y., Kim M., Yi S. K., Duc P.-A., Nantais J., et al., 2017, *ApJL*, 840, L7
- Slezak E., Durret F., Guibert J., Lobo C., 1998, *A&AS*, 128, 67
- Slezak E., Durret F., Guibert J., Lobo C., 1999, *A&AS*, 139, 559
- Solanes, J. M., Manrique, A., García-Gómez, C. et al. 2001, *ApJ*, 548, 97
- Spérone-Longin D., Jablonka P., Combes F., Castignani G., Rudnick G., Zaritsky D., et al., 2021, *A&A*, 647, A156
- Tacchella, S., Diemer, B., Hernquist, L., et al. 2019, *MNRAS*, 487, 5416
- Taylor G. B., Carilli C. L., Perley R. A., eds, 1999, *ASP Conf. Ser. Vol. 180, Synthesis Imaging in Radio Astronomy II*, Socorro NM
- Tonnesen S., 2019, *ApJ*, 874, 161
- Ulmer M. P., Adami C., Durret F., Ilbert O., Guennou L., 2011, *A&A*, 528, A36
- Venkatapathy Y., Bravo-Alfaro H., Mayya Y. D., Lobo C., Durret F., Gamez V., Valerdi M., et al., 2017, *AJ*, 154, 227
- Vollmer B., Soida M., Braine J., Abramson A., Beck R., Chung A., Crowl H. H., et al., 2012, *A&A*, 537, A143
- Walker I. R., Mihos J. C., Hernquist L., 1996, *ApJ*, 460, 121
- Wang J., Staveley-Smith L., Westmeier T., Cantinella B., Shao L., Reynolds T. N., For B. Q., et al., 2021, *ApJ*, 915, 70
- Xie L., De Lucia G., Hirschmann M., Fontanot F., 2020, *MNRAS*, 498, 4327

Table A1. The HI-detected galaxies in Abell 85

ID	Name	RA (2000)	Dec (2000)	Morph. type	g mag	color ($g-r$)	M_*	Opt-vel km s^{-1}	HI-vel km s^{-1}	Δv km s^{-1}	M_{HI} $10^9 M_{\odot}$	Def _{HI}		Dist. Mpc	HI pert.
(1)	(2)	(3)	(4)	(5)	(6)	(7)	(8)	(9)	(10)	(11)	(12)	Sa-Sb (13)	Sc-Irr (14)	(15)	(16)
1	323	00 42 18.7	-09 54 14	S?*	17.86	0.376	9.50	15618	15608	137	8.2	-0.27	-0.13	2.39	<i>N</i>
2	347	00 42 29.5	-10 01 07	S?*	17.62	0.352	9.59	15165	15175	91	2.5	-0.03	0.08	2.86	<i>N</i>
3	374	00 42 41.5	-08 56 49	S?*	16.39	0.512	10.26	15106	15107	318	13.8	-0.29	-0.14	1.60	<i>N</i>
4	986362 ^b	00 43 01.7	-09 47 34	-	17.27	0.418	9.79	15110	15107	227	6.5	-0.39	-0.27	2.23	<i>N</i>
5	461	00 43 14.3	-09 10 21	-	18.84	0.318	9.01	15015	15016	227	10.2	-0.85	-0.76	1.44	<i>N</i>
6	3114 ^a	00 43 19.5	-09 09 13	-	19.47	0.390	8.76	15060	15061	136	3.7	-0.46	-0.37	1.54	<i>N</i>
7	486	00 43 31.2	-09 51 48	S	16.81	0.288	9.82	16619	16615	230	7.2	-0.09	0.05	2.72	<i>N</i>
8	491	00 43 34.0	-08 50 37	S?*	17.05	0.297	9.94	14968	14993	182	11.6	-0.56	-0.44	2.43	<i>N</i>
9	496	00 43 38.7	-09 31 21	S?*	16.99	0.281	9.84	15004	14993	182	4.3	0.04	0.17	1.94	<i>Pos</i>
10	502	00 43 43.9	-09 04 23	-	17.30	0.340	9.73	15004	15038	182	11.8	-0.33	-0.19	2.03	<i>N</i>

Column (1): Sequence ID number.

Column (2): [DFL98] galaxy name (Durret et al. 1998); (^a) [SDG98] galaxy name (Slezak et al. 1998); (^b) PGC names (Paturel et al. 1989).

Columns (3) and (4): RA, Dec coordinates from NED.

Column (5): The morphological type from NED, except (*) taken from HyperLEDA.

Columns (6) and (7): The g magnitude and ($g-r$) color index estimated in this work from CFHT/PanSTARRS images.

Column (8): Stellar mass given by $\log(M_*/M_{\odot})$.

Column (9): Optical velocity from our redshift membership catalog (see Sect. 2).

Column (10): Heliocentric HI velocity. The uncertainty is taken as one-half the velocity resolution, *i.e.* $\sim 23 \text{ km s}^{-1}$ (see Table 3).

Column (11): The galaxy velocity width, the uncertainty is $\sim 46 \text{ km s}^{-1}$ (see Table 3).

Column (12): The HI-Mass following Haynes & Giovanelli (1984); uncertainties are lower than 10%; see the text for more details.

Columns (13) and (14): The upper and lower limits for HI deficiency, following Haynes & Giovanelli (1984).

Column (15): The projected cluster-centric distance considering the position of the corresponding BCG.

Column (16): Qualitative code indicating if the galaxy is normal in HI (*N*), otherwise it is perturbed. See the text for more details.

APPENDIX A: HI-DETECTED GALAXIES IN A85, A496, A2670.

Table A2. The HI-detected galaxies in Abell 496

ID	Name	RA (2000) (3)	Dec (2000) (4)	Morph. type (5)	g mag (6)	color ($g-r$) (7)	M_* (8)	Opt-vel km s^{-1} (9)	Hi-vel km s^{-1} (10)	Δv km s^{-1} (11)	M_{HI} $10^9 M_{\odot}$ (12)	Def _{HI} Sa-Sb (13)	Sc-Irr (14)	Dist. Mpc (15)	Hi pert. (16)
1	603	04 30 49.8	-13 12 28	-	16.92	0.193	9.29	9786	9724	88	1.7	-0.19	-0.11	1.63	<i>N</i>
2	672	04 31 03.4	-13 11 21	Sc	17.69	0.302	8.99	10776	10783	177	2.3	-0.14	-0.04	1.51	<i>N</i>
3	B042910.53-130437.3	04 31 30.0	-12 58 15	-	18.83	0.272	8.44	-	10407	44	1.9	-1.00	-0.97	1.42	<i>N</i>
4	853	04 31 32.0	-13 14 34	-	17.14	0.278	9.23	9208	9264	219	2.6	-0.22	-0.12	1.22	<i>N</i>
5	903***	04 31 40.3	-13 07 11	-	17.48	0.455	9.18	10904	-	-	>2.3	-	-	1.19	<i>N</i>
6	926***	04 31 43.1	-13 07 10	-	17.08	0.596	9.44	11106	-	-	>1.0	-	-	1.16	<i>N</i>
7	958	04 31 47.7	-12 44 23	-	19.38	0.224	8.16	-	10186	132	0.8	-0.16	-0.10	1.64	<i>N</i>
8	982	04 31 50.3	-12 43 54	-	17.68	0.174	8.93	10919	10871	89	1.0	-0.14	-0.06	1.64	<i>N</i>
9	989	04 31 51.8	-13 07 43	-	18.96	0.288	8.39	10006	10275	221	3.3	-0.38	-0.28	1.08	<i>Vel</i>
10	1054	04 32 02.8	-13 29 48	I	16.73	0.464	9.53	10289	9329	175	1.5	-0.03	0.07	1.08	<i>Vel, Pos</i>
11	1099	04 32 09.6	-12 41 42	Sc	15.70	0.584	10.07	10323	10319	309	7.3	-0.07	0.08	1.60	<i>N</i>
12	1169	04 32 20.4	-13 14 11	Sb	16.39	0.401	9.65	8990	8979	262	8.9	-0.52	-0.41	0.76	<i>N</i>
13	1179	04 32 21.8	-13 15 48	-	17.55	0.371	9.10	10057	10076	176	1.4	-0.15	-0.06	0.74	<i>N</i>
14	1275	04 32 41.8	-13 03 21	-	19.10	0.349	8.36	10608	10473	88	1.0	-0.17	-0.10	0.73	<i>Vel</i>
15	04.56-13.38**	04 32 45.3	-13 23 08	-	21.12	0.296	7.39	-	10694	88	0.6	-0.11	-0.05	0.59	<i>N</i>
16	1303	04 32 45.5	-12 33 39	-	19.68	0.399	8.12	-	9264	44	3.5	-1.20	-1.16	1.75	<i>N</i>
17	1315	04 32 48.1	-12 42 52	-	16.36	0.191	9.55	9954	9615	132	3.6	-0.17	-0.06	1.39	<i>Vel, Asy</i>
18	1324	04 32 49.0	-12 42 19	-	18.09	0.254	8.78	10037	9615	132	1.1	-0.16	-0.09	1.41	<i>Vel, Asy</i>
19	1338	04 32 51.1	-13 03 07	-	18.92	0.320	8.43	10474	10473	88	1.1	-0.33	-0.27	0.68	<i>N</i>
20	1354	04 32 54.2	-13 23 50	-	17.16	0.498	9.35	9932	9922	220	3.6	-0.62	-0.54	0.53	<i>N</i>
21	1363	04 32 54.7	-12 53 25	-	18.11	0.250	8.77	-	10385	88	2.5	-0.49	-0.41	0.98	<i>N</i>
22	04.55-13.06**	04 32 55.4	-13 03 33	-	21.33	0.484	7.40	-	10429	88	1.0	-0.78	-0.75	0.64	<i>N</i>
23	198 ^c	04 32 56.1	-13 36 38	Sc	15.65	0.709	10.16	11349	10561	177	2.5	-0.16	-0.06	0.92	<i>Vel</i>
24	3760	04 32 56.8	-12 46 41	SBbc	15.23	0.745	10.37	10602	10606	354	5.3	0.14	0.29	1.22	<i>Asy</i>
25	1386	04 32 59.8	-13 42 33	-	16.95	0.739	9.57	10557	10473	265	3.1	-0.10	0.01	1.13	<i>Asy</i>
26	1389	04 33 00.1	-13 57 28	-	19.65	0.535	8.21	-	10186	44	1.4	-0.71	-0.66	1.70	<i>N</i>
27	1399	04 33 02.0	-12 43 00	-	15.79	0.457	9.96	9361	9373	263	5.4	-0.59	-0.49	1.35	<i>N</i>
28	1418	04 33 05.3	-13 26 55	-	18.42	0.472	8.75	-	10473	89	1.2	-0.12	-0.03	0.55	<i>N</i>
29	1419	04 33 05.9	-13 59 54	-	18.84	0.860	8.75	10943	10971	266	1.6	0.36	0.47	1.79	<i>Def</i>
30	1457	04 33 10.9	-13 14 10	-	17.79	0.495	9.05	8991	8914	131	1.8	-0.32	-0.24	0.27	<i>Pos</i>
31	1461	04 33 11.4	-13 28 02	-	18.14	0.461	8.87	10670	10650	177	2.8	-0.54	-0.46	0.55	<i>N</i>
32	1474	04 33 13.7	-13 27 56	-	18.94	0.415	8.47	10159	10120	88	1.1	-0.31	-0.25	0.54	<i>N</i>
33	1482	04 33 15.1	-13 21 19	-	18.04	0.317	8.83	10207	10186	132	0.8	0.03	0.11	0.31	<i>N</i>
34	225 ^c	04 33 17.4	-12 59 01	Sb	15.61	0.674	10.16	10826	10915	266	0.6	0.35	0.44	0.70	<i>Def</i>
35	1512	04 33 19.6	-13 33 39	-	19.20	0.358	8.32	10268	10253	88	0.7	-0.17	-0.10	0.74	<i>N</i>
36	1547	04 33 23.3	-13 20 21	Sc	16.89	0.504	9.48	10188	10208	265	3.8	-0.27	-0.17	0.23	<i>N</i>
37	1549	04 33 23.9	-13 31 03	S	16.74	0.590	9.59	10228	10231	397	10.4	-0.75	-0.64	0.63	<i>N</i>
38	1565	04 33 25.4	-13 41 09	Sc	16.75	0.524	9.55	10866	10827	354	3.1	-0.12	0.00	1.02	<i>Pos</i>
39	1584	04 33 29.0	-13 41 15	-	20.40	0.273	7.72	9443	9527	44	0.4	0.31	0.39	1.02	<i>Def</i>
40	1624	04 33 34.6	-12 38 34	-	19.40	0.329	8.21	-	10539	133	1.4	-0.22	-0.14	1.48	<i>N</i>
41	1656***	04 33 38.5	-13 35 46	I	16.98	0.411	9.38	11194	-	-	>0.9	-	-	0.80	<i>N</i>
42	1709	04 33 44.7	-13 33 50	I	17.07	0.523	9.40	9779	9724	176	1.2	0.23	0.33	0.72	<i>Def, Pos</i>
43	1747***	04 33 50.9	-13 44 18	-	18.62	0.400	8.61	11037	-	-	>0.8	-	-	1.15	<i>N</i>
44	1834	04 34 02.0	-13 17 49	Sbc	15.89	0.470	9.92	10347	10319	132	2.3	-0.01	0.10	0.25	<i>N</i>
45	1849	04 34 04.1	-12 48 52	-	18.56	0.356	8.62	9002	9023	88	1.1	-0.02	0.07	1.10	<i>N</i>
46	1860***	04 34 06.3	-13 39 44	-	19.40	0.476	8.29	11267	-	-	>1.8	-	-	1.00	<i>N</i>
47	1967	04 34 23.9	-13 15 32	-	18.16	0.405	8.83	9480	9483	132	0.7	0.08	0.15	0.45	<i>N</i>
48	2036	04 34 36.8	-12 45 30	-	19.08	0.128	8.25	9936	9944	88	1.5	-0.49	-0.43	1.33	<i>N</i>
49	2246	04 35 10.5	-13 59 34	-	18.01	0.685	9.03	-	10451	132	3.0	-0.56	-0.48	1.96	<i>N</i>
50	2252	04 35 11.0	-13 45 18	-	17.97	0.446	8.94	10963	11004	87	2.9	-0.32	-0.23	1.49	<i>N</i>
51	B043258.99-130504.4	04 35 18.3	-12 58 58	-	20.78	0.554	7.70	-	10054	44	1.3	-0.47	-0.41	1.18	<i>N</i>
52	2447	04 35 45.5	-13 58 37	-	17.86	0.694	9.09	-	10606	265	4.3	-0.34	-0.24	2.11	<i>Asy</i>
53	2485	04 35 52.0	-13 19 47	Sab	16.10	0.810	10.00	10301	10363	309	1.4	0.43	0.55	1.31	<i>Def, Pos</i>
54	2503	04 35 54.5	-13 34 49	S0-a	19.29	0.472	8.34	-	10385	88	0.8	-0.53	-0.49	1.53	<i>N</i>
55	2516	04 35 56.7	-13 19 49	-	18.70	0.331	8.54	10609	10584	133	1.0	-0.11	-0.03	1.36	<i>N</i>
56	2525	04 35 57.8	-13 43 56	-	19.65	0.604	8.25	-	10385	177	1.3	-0.15	-0.07	1.76	<i>N</i>
57	2534	04 35 59.5	-13 18 07	Sab	16.06	0.830	10.03	10188	10098	220	0.9	0.55	0.67	1.38	<i>Def</i>
58	04.60-13.55**	04 36 14.2	-13 33 20	-	-	-	-	-	10960	44	0.8	-0.76	-0.73	1.66	<i>N</i>

Column (1): Sequence ID number.

Column (2): [SDG99]-SRC galaxy name (Slezak et al. 1999); (^c) [DFL99] galaxy name (Durret et al. 1999); (**) The names were constructed using RA, Dec in hours and decimal degrees, they are objects not cataloged in NED, and the coordinates shown for these objects are those of the HI emission. (***) The emission extends beyond the observed range.

Columns (3) and (4): RA, Dec coordinates from NED.

Column (5): The morphological type from NED.

Columns (6) and (7): The g magnitude and ($g-r$) color index estimated in this work from CFHT/PanSTARRS images.

Column (8): Stellar mass given by $\log(M_*/M_{\odot})$

Column (9): Optical velocity from our redshift membership catalog (see Sect. 2).

Column (10): Heliocentric HI velocity. The uncertainty is taken as one-half the velocity resolution, i.e. $\sim 22 \text{ km s}^{-1}$ (see Table 3).

Column (11): The galaxy velocity width, the uncertainty is $\sim 44 \text{ km s}^{-1}$ (see Table 3).

Column (12): The HI-Mass following Haynes & Giovanelli (1984); uncertainties are lower than 10%; see the text for more details.

Columns (13) and (14): The upper and lower limits for HI deficiency, following Haynes & Giovanelli (1984).

Column (15): The projected cluster-centric distance considering the position of the corresponding BCG.

Column (16): Qualitative code indicating the HI appearance, either normal or perturbed. See the text for more details.

APPENDIX B: SPIRALS NOT DETECTED IN HI, A85, A496, A2670

Table A3. The HI-detected galaxies in Abell 2670

ID	Name	RA (2000)	Dec (2000)	Morph. type	g mag	color ($g-r$)	M_*	Opt-vel km s ⁻¹	HI-vel km s ⁻¹	Δv km s ⁻¹	M_{HI} 10 ⁹ M _⊙	Def _{HI} Sa-Sb	Def _{HI} Sc-Irr	Dist. Mpc	HI pert.
(1)	(2)	(3)	(4)	(5)	(6)	(7)	(8)	(9)	(10)	(11)	(12)	(13)	(14)	(15)	(16)
1	J235222.31-104134.7	23 52 22.3	-10 41 35	-	19.03	0.364	9.28	22814	22666	238	5.4	-0.47	-0.36	2.81	<i>Vel, Pos</i>
2	J235232.39-104154.1	23 52 32.4	-10 41 54	-	19.35	0.249	9.07	-	22595	95	4.4	-0.57	-0.48	2.65	<i>N</i>
3	J235233.13-103640.8	23 52 33.1	-10 36 41	-	18.34	0.388	9.62	22724	22690	191	4.8	-0.35	-0.24	2.40	<i>Pos</i>
4	J235247.36-105259.1	23 52 47.3	-10 52 59	E?*	16.78	0.640	10.51	22721	22714	143	6.6	0.19	0.35	3.08	<i>Def, Pos</i>
5	3325027 ^b	23 52 55.8	-10 42 04	-	19.16	0.354	9.21	21795	21929	95	2.6	-0.20	-0.10	2.24	<i>N</i>
6	J235303.74-110454.9	23 53 03.7	-11 04 55	S?*	16.30	0.679	10.76	22823	22738	191	7.0	-0.01	0.14	3.82	<i>N</i>
7	J235305.67-104055.6	23 53 05.7	-10 40 56	Sbc	16.51	0.434	10.49	21930	21953	427	14.4	-0.31	-0.17	2.02	<i>N</i>
8	J235308.87-104417.3	23 53 08.9	-10 44 17	E?	17.96	0.802	10.06	22578	22547	667	25.6	-0.60	-0.46	2.19	<i>N</i>
9	J235310.49-104142.3	23 53 10.5	-10 41 42	-	20.00	0.267	8.78	-	21858	142	3.6	-0.79	-0.72	2.00	<i>N</i>
10	J235310.87-110203.0	23 53 10.9	-11 02 03	S?*	17.33	0.684	10.29	22806	22785	96	3.4	0.12	0.25	3.52	<i>Def</i>
11	J235319.07-102303.2	23 53 19.1	-10 23 03	Sc	17.07	0.614	10.36	22300	22305	236	4.2	0.13	0.27	1.19	<i>Def</i>
12	J235320.90-101047.7	23 53 20.9	-10 10 48	-	18.67	0.352	9.44	22306	22423	283	2.7	-0.06	0.05	1.70	<i>N</i>
13	24FGRS S888Z177	23 53 20.9	-10 32 39	-	19.14	0.445	9.28	23114	23298	142	3.0	-0.29	-0.20	1.31	<i>Vel</i>
14	J235324.23-104916.6	23 53 24.2	-10 49 17	-	17.70	0.330	9.88	21947	21976	190	7.1	-0.67	-0.58	2.38	<i>Pos, Asy</i>
15	J235326.38-101549.0	23 53 26.4	-10 15 49	E?*	18.22	0.603	9.82	22410	22399	425	12.6	-0.11	0.04	1.31	<i>N</i>
16	J235338.22-105443.9	23 53 38.2	-10 54 44	S?*	17.47	0.589	10.16	22484	22476	143	6.7	-0.22	-0.09	2.71	<i>Pos</i>
17	J235339.45-102430.7	23 53 39.4	-10 24 30	-	20.11	0.302	8.74	-	22588	142	2.6	-0.44	-0.35	0.72	<i>N</i>
18	J235339.87-102547.6	23 53 39.9	-10 25 48	Sa	17.26	0.552	10.23	22552	22612	189	2.6	0.16	0.28	0.73	<i>Def, Pos</i>
19	J235341.02-103453.9	23 53 41.0	-10 34 54	-	19.93	0.375	8.87	-	21482	188	3.2	-0.57	-0.49	1.11	<i>N</i>
20	J235344.08-104041.2	23 53 44.1	-10 40 41	-	20.54	0.544	8.70	-	23575	48	2.1	-0.51	-0.45	1.51	<i>N</i>
21	J235346.66-101614.8	23 53 46.7	-10 16 15	Sab	16.31	0.629	10.73	23796	23964	143	3.7	0.36	0.52	0.97	<i>Def, Vel, Pos</i>
22	J235356.57-101510.4	23 53 56.6	-10 15 10	Sd	17.07	0.495	10.28	21565	21529	94	2.2	-0.51	-0.44	0.94	<i>N</i>
23	141225 ^b	23 53 57.1	-10 22 29	Sa	17.31	0.509	10.17	21898	21834	423	10.6	-0.46	-0.33	0.43	<i>N</i>
24	141233 ^b	23 53 58.5	-10 28 27	-	19.26	0.360	9.17	22168	22140	283	5.0	-0.56	-0.47	0.44	<i>N</i>
25	J235411.73-102115.1	23 54 11.7	-10 21 15	-	19.26	0.375	9.18	24268	24321	95	2.3	-0.30	-0.21	0.35	<i>N</i>
26	J235413.59-102748.2	23 54 13.6	-10 27 48	E?	17.79	0.563	9.99	24568	24536	143	1.7	0.03	0.14	0.24	<i>N</i>
27	J235418.24-101349.5	23 54 18.2	-10 13 50	Sc	17.43	0.580	10.17	23251	23227	474	11.0	0.08	0.25	1.00	<i>Def</i>
28	J235419.51-103300.3	23 54 19.5	-10 33 00	Sa	16.77	0.601	10.49	23925	23964	429	11.5	-0.25	-0.11	0.71	<i>Asy, Pos</i>
29	J235435.77-095748.6	23 54 35.8	-09 57 49	S?*	17.94	0.370	9.79	23442	23407	144	9.2	-0.30	-0.17	2.46	<i>N</i>
30	J235438.15-101907.6	23 54 38.1	-10 19 08	Sab	16.76	0.523	10.44	22506	22517	378	10.0	-0.19	-0.05	0.75	<i>Asy</i>
31	J235444.17-101655.9	23 54 44.2	-10 16 56	Scd	17.00	0.426	10.26	23184	23120	383	7.3	-0.01	0.14	0.98	<i>Pos</i>
32	J235446.43-095752.9	23 54 46.4	-09 57 53	-	17.73	0.780	10.16	22768	22666	334	4.6	-0.05	0.07	2.50	<i>N</i>
33	J235449.71-100151.0	23 54 49.7	-10 01 51	-	18.43	0.466	9.63	-	21857	237	2.7	0.36	0.50	2.20	<i>Def, Pos</i>
34	J235451.55-101238.9	23 54 51.5	-10 12 39	-	19.13	0.253	9.17	23284	23216	191	3.2	-0.27	-0.17	1.37	<i>N</i>
35	J235453.62-101931.6	23 54 53.6	-10 19 32	Im	18.13	0.505	9.79	21818	21787	235	4.5	-0.24	-0.12	0.99	<i>Pos</i>
36	J235454.17-101717.0	23 54 54.2	-10 17 17	Sc	15.83	0.544	10.89	23065	23168	478	10.9	-0.01	0.15	1.12	<i>Asy</i>
37	J235607.62-095938.1	23 56 07.6	-09 59 38	E*	17.00	0.670	10.43	23035	23168	96	2.8	0.31	0.44	3.34	<i>Def, Pos</i>
38	J235619.93-101246.2	23 56 19.9	-10 12 46	S?*	16.23	0.507	10.67	22923	22953	430	10.2	-0.20	-0.06	2.95	<i>N</i>

Column (1): Sequence ID number.

Columns (2): SDSS names; (^b) PGC names (Paturol et al. 1989).

Columns (3) and (4): RA, Dec coordinates from NED.

Column (5): The morphological type from NED, except (*) taken from HyperLEDA.

Columns (6) and (7): The g magnitude and ($g-r$) color index estimated in this work from CFHT/PanSTARRS images.

Column (8): Stellar mass given by $\log(M_*/M_\odot)$.

Column (9): Optical velocity from our redshift membership catalog (see Sect. 2).

Column (10): Heliocentric HI velocity. The uncertainty is taken as one-half the velocity resolution, i.e. ~ 24 km s⁻¹ (see Table 3).

Column (11): The galaxy velocity, the uncertainty is ~ 48 km s⁻¹ (see Table 3).

Column (12): The HI-Mass following Haynes & Giovanelli (1984); uncertainties are lower than 10%; see the text for more details.

Columns (13) and (14): The upper and lower limits for HI deficiency, following Haynes & Giovanelli (1984).

Column (15): The projected cluster-centric distance considering the position of the corresponding BCG.

Column (16): Qualitative code indicating the HI appearance, either normal or perturbed. See the text for more details.

Table B1. Catalog of bright spirals (B-Sp) not detected in HI in Abell 85

ID	Name	RA (2000)	Dec (2000)	Morph. type	Opt-vel km s ⁻¹	<i>g</i> mag	color (<i>g</i> - <i>r</i>)	M _*	Dist. Mpc
(1)	(2)	(3)	(4)	(5)	(6)	(7)	(8)	(9)	(10)
1	044	00 39 47.6	-09 48 11	-	15848	18.34	0.493	9.34	2.77
2	046	00 39 48.4	-09 14 37	S?*	17338	17.78	0.596	9.67	1.97
3	052	00 39 59.1	-09 26 04	S?*	16939	18.07	0.434	9.44	1.85
4	920 ^a	00 40 01.9	-10 06 05	-	17458	18.53	0.433	9.22	3.56
5	93148 ^b	00 40 13.6	-08 58 01	-	17935	18.10	0.311	9.34	2.03
6	070	00 40 18.7	-08 52 57	S0/a	17923	15.99	0.695	10.56	2.20
7	087	00 40 40.9	-08 48 59	-	15652	18.15	0.393	9.37	2.20
8	099	00 40 51.6	-09 20 28	-	16506	18.82	0.536	9.15	0.95
9	127	00 41 10.4	-09 15 01	-	18254	18.45	0.480	9.29	0.67
10	128	00 41 11.1	-09 55 30	S?*	17000	18.40	0.556	9.36	2.50
11	133	00 41 12.8	-09 32 04	S?*	17139	16.40	0.584	10.30	1.08
12	139	00 41 14.2	-08 55 54	S?*	15157	17.83	0.324	9.48	1.56
13	145	00 41 19.0	-09 23 24	S?*	14935	17.94	0.442	9.50	0.61
14	151	00 41 21.3	-08 43 30	S?*	16050	18.02	0.524	9.51	2.30
15	167	00 41 27.1	-09 13 43	S?*	14167	16.46	0.517	10.23	0.47
16	170	00 41 27.9	-09 23 30	S?*	14836	18.18	0.555	9.46	0.50
17	1645 ^a	00 41 27.9	-09 13 47	-	16258	17.36	0.555	9.84	0.46
18	201	00 41 36.2	-08 59 35	E?*	17935	16.89	0.338	9.92	1.23
19	218	00 41 42.5	-09 21 26	-	14737	18.56	0.576	9.29	0.25
20	1875 ^a	00 41 44.4	-09 26 25	-	17457	18.16	0.527	9.45	0.54
21	226	00 41 45.5	-09 40 33	S?*	17072	17.61	0.487	9.68	1.45
22	1940 ^a	00 41 49.0	-09 57 05	S?*	15537	16.58	0.486	10.16	2.52
23	246	00 41 50.8	-09 13 46	-	18178	18.37	0.321	9.23	0.29
24	255	00 41 53.3	-09 29 31	E?*	15732	16.38	0.342	10.16	0.74
25	256	00 41 53.4	-09 38 46	-	15924	18.81	0.397	9.07	1.34
26	267	00 41 57.4	-09 35 24	S?*	15918	17.22	0.551	9.90	1.12
27	273	00 41 59.8	-09 42 32	-	15506	17.98	0.375	9.44	1.59
28	2146 ^a	00 41 59.9	-09 39 10	S0	15780	16.42	0.455	10.21	1.37
29	276	00 42 00.7	-09 50 04	S	15627	16.21	0.679	10.45	2.07
30	286	00 42 05.0	-09 32 04	Sc	15852	15.93	0.532	10.49	0.93
31	292	00 42 06.4	-09 33 35	-	16097	18.71	0.460	9.15	1.03
32	2260 ^a	00 42 08.4	-09 31 05	-	16963	18.69	0.570	9.23	0.88
33	2276 ^a	00 42 09.8	-09 28 52	-	16739	18.19	0.273	9.28	0.76
34	304	00 42 11.7	-09 58 14	S?*	16191	18.30	0.515	9.38	2.62
35	316	00 42 17.3	-09 28 48	S?*	15855	17.14	0.535	9.93	0.81
36	321	00 42 18.5	-09 39 12	-	15449	17.91	0.311	9.43	1.43
37	325	00 42 19.9	-09 25 28	S?*	15341	18.01	0.501	9.51	0.67
38	338	00 42 24.2	-09 16 17	S?*	18195	17.02	0.576	10.01	0.55
39	345	00 42 28.4	-09 49 38	S?*	15006	18.42	0.557	9.35	2.13
40	355	00 42 32.9	-09 21 44	-	17064	18.94	0.356	8.98	0.72
41	356	00 42 33.8	-08 52 53	Sc	17722	16.79	0.697	10.19	1.78
42	358	00 42 33.9	-09 08 46	S?*	16677	17.16	0.600	9.96	0.92
43	362	00 42 34.7	-09 04 36	S?*	14745	17.48	0.451	9.72	1.13
44	366	00 42 37.0	-09 45 20	-	17065	18.64	0.559	9.25	1.91
45	382	00 42 43.9	-09 44 21	Sb	15231	17.02	0.660	10.06	1.90
46	391	00 42 48.4	-09 34 41	S?*	17940	17.63	0.500	9.68	1.41
47	413	00 42 58.7	-08 55 06	-	17081	18.57	0.520	9.26	1.85
48	429	00 43 04.2	-09 32 43	Sc	15812	17.25	0.618	9.93	1.51
49	435	00 43 06.0	-09 50 15	Sb	14742	16.66	0.650	10.22	2.40
50	439	00 43 08.2	-09 49 37	-	15203	17.39	0.690	9.91	2.39
51	2972 ^a	00 43 08.1	-09 34 44	-	15024	18.13	0.403	9.39	1.64
52	2997 ^a	00 43 09.8	-10 04 43	-	15960	18.09	0.395	9.40	3.27
53	449	00 43 11.0	-09 18 00	-	15945	18.94	0.511	9.08	1.29
54	451	00 43 11.6	-09 38 16	Se	16253	15.84	0.586	10.57	1.84
55	483	00 43 30.5	-09 43 59	S?*	15125	16.80	0.516	10.08	2.31
56	514	00 44 04.1	-09 41 06	-	14934	18.83	0.290	8.99	2.60

Column (1): Sequence ID number.

Column (2): [DFL98] galaxy name (Durret et al. 1998); (^a) [SDG98] galaxy name (Slezak et al. 1998); (^b) PGC names (Paturel et al. 1989).

Columns (3) and (4): RA, Dec coordinates from NED.

Column (5): The morphological type from NED, except (*) taken from HyperLEDA.

Column (6): Optical velocity from our redshift membership catalog (see Sect. 2).

Columns (7) and (8): The *g* magnitude and (*g* - *r*) color index estimated in this work from CFDP/PanSTARRS images.

Column (9): Stellar mass given by log(M_{*}/M_⊙).

Column (10): The cluster-centric distance from the BCG position.

Table B2. Catalog of bright spirals (B-Sp) not detected in HI in Abell 496

ID	Name	RA (2000)	Dec (2000)	Morph. type	Opt-vel km s ⁻¹	<i>g</i> mag	color (<i>g</i> − <i>r</i>)	M _*	Dist. Mpc
(1)	(2)	(3)	(4)	(5)	(6)	(7)	(8)	(9)	(10)
1	576	04 30 45.1	-12 37 39	S0-a*	9325	15.04	0.793	10.47	2.26
2	671	04 31 03.1	-12 58 26	SBb*	10524	14.40	0.438	10.60	1.65
3	718	04 31 10.7	-12 39 20	-	9115	16.51	0.588	9.69	2.04
4	799	04 31 23.7	-13 04 13	E?*	9587	15.80	0.508	9.98	1.38
5	924	04 31 42.9	-12 32 38	-	9519	17.75	0.568	9.12	2.05
6	B042925.77-124531.4	04 31 45.6	-12 39 10	-	8656	17.70	0.119	8.93	1.82
7	1080	04 32 06.6	-13 04 59	Sc	10840	17.12	0.737	9.49	0.98
8	1193	04 32 24.0	-12 46 48	SBa	10140	15.89	0.735	10.06	1.36
9	1216	04 32 27.7	-12 38 43	-	10339	16.46	0.620	9.70	1.62
10	1443	04 33 08.9	-13 02 36	Sbc	10197	17.18	0.651	9.42	0.59
11	1520	04 33 20.2	-13 26 22	SBb	9937	16.59	0.707	9.72	0.46
12	1660	04 33 38.7	-12 32 04	E?*	9812	15.20	0.519	10.27	1.74
13	2193	04 35 03.0	-12 53 51	SBab	9591	15.90	0.734	10.05	1.20
14	2195	04 35 03.7	-13 39 20	Sa	9577	16.97	0.893	9.62	1.26
15	2210	04 35 05.9	-13 10 54	-	10230	16.86	0.409	9.46	0.88
16	2253	04 35 11.1	-13 14 40	SBab	10575	15.27	0.744	10.35	0.91
17	2374	04 35 32.4	-13 33 23	SBaa	10121	16.46	0.928	9.89	1.31

Column (1): Sequence ID number.

Column (2): [SDG99]-SRC galaxy name (Slezak et al. 1999).

Columns (3) and (4): RA, Dec coordinates from NED.

Column (5): The morphological type from NED, except (*) taken from HyperLEDA.

Column (6): Optical velocity from our redshift membership catalog (see Sect. 2).

Columns (7) and (8): The *g* magnitude and (*g* − *r*) color index estimated in this work from CFHT/PanSTARRS images.

Column (9): Stellar mass given by log(M_{*}/M_⊙).

Column (10): The cluster-centric distance from the BCG position.

Table B3. Catalog of bright spirals (B-Sp) not detected in HI in Abell 2670

ID	Name	RA	Dec	Morph.	Opt-vel	g	color	M_*	Dist.
(1)	(2)	(2000)	(2000)	type	km s^{-1}	mag	($g - r$)	(9)	Mpc
		(3)	(4)	(5)	(6)	(7)	(8)		(10)
1	J235258.26-105430.3	23 52 58.3	-10 54 30	S?*	23588	18.08	0.493	9.81	3.06
2	J235258.58-104111.7	23 52 58.6	-10 41 12	S?*	21817	16.70	0.627	10.54	2.16
3	J235303.21-101748.0	23 53 03.2	-10 17 48	Sbc	22296	17.53	0.522	10.08	1.66
4	J235311.63-101835.4	23 53 11.6	-10 18 35	S?*	21754	17.98	0.539	9.89	1.46
5	J235326.80-102442.1	23 53 26.8	-10 24 42	S?*	21684	17.86	0.360	9.82	1.02
6	J235344.11-102200.7	23 53 44.1	-10 22 01	-	24283	18.92	0.101	9.20	0.70
7	J235356.81-100930.2	23 53 56.8	-10 09 30	-	23204	19.05	0.387	9.29	1.43
8	J235357.29-102550.0	23 53 57.3	-10 25 50	-	22168	19.29	0.319	9.13	0.36
9	J235358.85-104130.7	23 53 58.9	-10 41 31	S?*	22207	17.51	0.334	9.97	1.48
10	J235405.85-102624.5	23 54 05.9	-10 26 25	-	21388	19.44	0.513	9.19	0.20
11	141266 ^b	23 54 08.9	-10 27 49	-	22108	18.97	0.564	9.45	0.26
12	J235414.84-102448.8	23 54 14.8	-10 24 49	-	21178	17.31	0.728	10.32	0.04
13	J235416.65-101454.6	23 54 16.7	-10 14 55	Sd	22630	16.42	0.598	10.65	0.90
14	J235420.58-100813.5	23 54 20.6	-10 08 14	-	24458	19.06	0.332	9.25	1.50
15	J235422.17-102022.4	23 54 22.2	-10 20 22	-	21208	19.26	0.458	9.23	0.46
16	J235425.88-095923.7	23 54 25.9	-09 59 24	E?*	22779	17.93	0.639	9.98	2.29
17	J235431.44-100210.2	23 54 31.5	-10 02 10	-	22283	19.01	0.379	9.30	2.06
18	J235434.57-095415.5	23 54 34.6	-09 54 16	-	23284	19.22	0.484	9.27	2.76
19	J235436.64-095802.9	23 54 36.7	-09 58 03	-	22294	18.87	0.455	9.42	2.44
20	J235436.83-101758.1	23 54 36.8	-10 17 58	S0/a	23244	18.04	0.508	9.84	0.81
21	J235439.40-100006.0	23 54 39.4	-10 00 06	-	21916	18.22	0.457	9.72	2.28
22	J235445.81-101445.5	23 54 45.8	-10 14 46	Sd	23371	17.52	0.449	10.04	1.15
23	J235506.02-103351.3	23 55 06.0	-10 33 51	-	23359	18.23	0.391	9.67	1.37
24	J235509.50-100353.1	23 55 09.5	-10 03 53	-	21885	18.19	0.434	9.72	2.23
25	J235514.23-103611.3	23 55 14.2	-10 36 11	-	23375	19.09	0.393	9.27	1.63
26	J235514.70-102947.5	23 55 14.7	-10 29 48	S0/a	24533	17.76	0.645	10.06	1.39
27	J235517.83-095359.8	23 55 17.8	-09 53 60	-	22762	18.57	0.453	9.55	3.08
28	J235526.62-100843.4	23 55 26.6	-10 08 43	-	21724	18.75	0.371	9.41	2.14

Column (1): Sequence ID number.

Column (2): SDSS names; (^b) PGC names (Paturol et al. 1989).

Columns (3) and (4): RA, Dec coordinates from NED.

Column (5): The morphological type from NED, except (*) taken from HyperLEDA.

Column (6): Optical velocity from our redshift membership catalog (see Sect. 2).

Columns (7) and (8): The g magnitude and ($g - r$) color index estimated in this work from CFHT/PanSTARRS images.

Column (9): Stellar mass given by $\log(M_*/M_\odot)$.

Column (10): The cluster-centric distance from the BCG position.